Journal of Computational Science 55 (2021) 101470

Contents lists available at ScienceDirect

Journal of Computational Science

journal homepage: www.elsevier.com/locate/jocs

Efficient momentum conservation constrained PDE-LDDMM with Gauss–Newton–Krylov optimization, Semi-Lagrangian Runge–Kutta solvers, and the band-limited parameterization ☆

Monica Hernandez

University of Zaragoza, Spain

ARTICLE INFO

Keywords:
PDE-LDDMM
EPDiff equation
Adjoint Jacobi equations
Gauss–Newton–Krylov optimization
Semi-Lagrangian integration
Band-limited vector fields
Optimal control

ABSTRACT

This paper proposes three efficient variants of Jacobi EPDiff PDE-LDDMM, where efficiency is achieved through Semi-Lagrangian Runge–Kutta integration and the band-limited parameterization. During Gauss–Newton–Krylov optimization, the method computes the gradient and the Hessian-vector product on the final time sample, and transports these magnitudes towards the initial time using the adjoint Jacobi equations and their incremental counterparts. Then, the optimization is performed on the initial time sample. The proposed methods have effectively achieved a considerable reduction of the computational complexity at a competitive accuracy. These variants constitute a contribution to the efficient computation of diffeomorphisms belonging to geodesics, suitable for statistical shape analysis or the construction of transversal and longitudinal models of shape variability using Principal Geodesic Analysis and Geodesic Regression in spaces of diffeomorphisms.

1. Introduction

In the last 20 years, Computational Anatomy has been established as a powerful interdisciplinary field for the transversal and longitudinal analysis of shape variability [1,2]. The discipline of Computational Anatomy is based on Sir D'Arcy Thompson's original ideas for explaining the similarity of the anatomical shape of homologous species using the transformations existing between the anatomical structures [3]. In Computational Anatomy, shape similarity is measured from the diffeomorphic transformations estimated between the anatomies. The Riemannian manifold of diffeomorphisms and its Lie group structure provides a metric space where a generative model can be defined from the tangent space for the analysis of shape variability from diffeomorphisms. This model has been useful to understand and quantify different diseases from their effects in the shape of the affected organs [4,5]. This particular approach has shown very promising results in the characterization of brain degeneration in Alzheimer's disease [6], and it may extend its applications from medical imaging to various domains in computer vision and computer graphics.

1.1. Diffeomorphisms, geodesics, and momentum conservation constrained LDDMM

Diffeomorphisms are computed from the anatomical images using diffeomorphic registration methods. There exists a vast literature on diffeomorphic registration methods with differences in the variational formulation of the problem, diffeomorphism parameterization, optimization methods, and additional constraints [7,8]. Even the most recent proposals based on deep-learning use these variational formulations and the different diffeomorphism parameterizations in the definition of the loss functions while optimization is approached using training data in supervised or unsupervised ways [9–15]. Although the differentiability and invertibility of the transformations constitute crucial features for some Computational Anatomy applications, the computation of diffeomorphisms belonging to geodesics is fundamental for a mathematically correct approach to perform statistical shape analysis [16] or to build transversal and longitudinal models of shape variability using Principal Geodesic Analysis and Geodesic Regression in spaces of diffeomorphisms [4,5].

From the different diffeomorphism parameterizations in the literature, pioneering Large Deformation Diffeomorphic Metric Mapping (LDDMM) [17] was proposed from the minimization of a variational

☆ This work was partially supported by the National research grants TIN2016-80347-R (DIAMOND project) and PID2019-104358RB-I00 (DL-Aging project), Government of Aragon Group Reference T64_20R (COS2MOS research group), and NVIDIA through the Barcelona Supercomputing Center (BSC) GPU Center of Excellence.

E-mail address: mhg@unizar.es.

https://doi.org/10.1016/j.jocs.2021.101470
Received 13 November 2020; Received in revised form 27 August 2021; Accepted 28 September 2021
Available online 15 October 2021

problem formulated on time-varying velocity field flows (i.e. non-stationary parameterization). The critical points of the regularization energy are critical points of the length functional with the additional property of constant speed [17,18]. Provided that the image similarity energy is zero at convergence (i.e. exact matching), the solution to the LDDMM problem would be a geodesic. In practice, registration is usually an inexact matching problem. The solutions depart from belonging to geodesic paths due to the underconstrained model used for time-varying velocity fields and numerical errors inherent to the differences of the images existing between individuals. Therefore, the simple non-stationary parameterization for diffeomorphism representation does not provide proper geodesic paths [17,19].

The original LDDMM variational formulation can be parameterized in the initial velocity field under the Euler–Poincare differential (EPDiff) equation [20] or the momentum conservation equation [21]. Both constraints have shown to be equivalent since the solutions of the EPDiff equation have the momentum conservation property and they allow the computation of geodesic paths of diffeomorphisms for the inexact matching problem with geodesic shooting. To date, the approaches based on the solution of the EPDiff equation are preferable for momentum conservation constrained LDDMM since derivations can be performed in the tangent space avoiding more complicated algebraic manipulations in the diffeomorphism manifold [19,20,22–25].

1.2. PDE-constrained LDDMM

An important branch of current research in diffeomorphic registration is focused on physically meaningful methods [26–30]. In many clinical applications, deformations are known to follow biophysically constrained models. For example, normal cardiac motion is incompressible [26]. This means that the Jacobian determinant of the transformations is equal to one. The motion of some organs in the abdominal cavity such as the liver or the kidneys is nearly incompressible. Models of evolution of brain tumors undergo complicated biophysical priors [31–33]. The expanding and contracting lung during respiration follows a sliding motion in the boundary [27]. These applications would be benefit from a specific biophysically constrained framework for diffeomorphic registration.

PDE-constrained Large Deformation Diffeomorphic Metric Mapping (PDE-LDDMM) has become relevant in the last decade for the computation of transformations under plausible physical models. In the original proposal by Hart et al. the problem is modeled using a PDE-constrained variational formulation based on the non-stationary parameterization of diffeomorphisms [34]. The constrained optimization approach provides the versatility to impose different physical models to the computed transformations by just adding the PDEs associated with the problem as hard constraints. Thus, PDE-LDDMM can be formulated to control the compressibility of the deformation map from incompressible to nearly incompressible models and additional constraints have been proposed to control the shear of the transformation [29].

In particular, the combination of Gauss–Newton–Krylov for optimization, with spectral methods for differentiation, and Runge–Kutta schemes for PDE integration, proposed in Mang et al. works [28,29], shows excellent numerical accuracy and a fast convergence rate. The computational complexity of PDE-LDDMM methods due to the use of RK schemes for PDE integration has been reduced thanks to the use of Semi-Lagrangian Runge–Kutta (SL-RK) PDE integration [35–37], the band-limited vector field parameterization [38,39], or the combination of both [40]. With SL-RK schemes, the time sampling needed for stability is much smaller than the sampling typically needed with explicit schemes, yielding to a considerable reduction of the computational complexity of the problem [40]. The band-limited parameterization has also shown an important reduction of the computational complexity of different LDDMM problems with an affordable penalty on the accuracy of the registration results [24,38,39]. However, these methods have mostly been proposed with the stationary and non-stationary parameterization of diffeomorphisms, limiting their applicability to areas where geodesics are not needed.

1.3. Momentum conservation constrained PDE-LDDMM

The EPDiff equation can be imposed as a physical constraint in PDE-LDDMM providing diffeomorphisms with the momentum conservation property. Momentum conservation constrained (MCC) PDE-LDDMM methods like [19,22,23,25] have been proposed for the tasks of diffeomorphic registration, geodesic regression, and registration uncertainty quantification. These methods are based on the original ideas of Hart et al. [34]. MCC PDE-LDDMM is formulated in the space of initial velocity fields and includes the EPDiff equation in the hard constraints of the problem [41]. The EPDiff physical constraint imposes the momentum conservation property and guarantees that the obtained diffeomorphisms belong to geodesic paths. Most MCC PDE-LDDMM methods use gradient-descent in the optimization due to the complex dependence of the energy functional on the initial velocity field [19,22,23].

Gauss–Newton–Krylov optimization has been successfully proposed in Jacobi EPDiff PDE-LDDMM [25]. The gradient and the Hessian-vector products are derived on the final time sample. These magnitudes are transported backward using the adjoint and the incremental adjoint Jacobi equations and used in the update of the initial velocity field. Jacobi EPDiff PDE-LDDMM departs substantially from MCC PDE-LDDMM methods [19,22,23] by:

- The use of Gauss–Newton–Krylov optimization vs gradient descent.
- The derivation on the final time sample vs the derivation on the initial time sample.
- The transport of gradient and Hessian-vector products toward the initial time sample.

The idea of transporting the derivations on the final time sampling, originally proposed in [24,42] for MCC LDDMM with gradient-descent optimization, avoids the complex dependence on the initial velocity field in the computations and increases the stability of the computations through the iterations. Indeed, Jacobi EPDiff PDE-LDDMM has shown to overpass Vialard et al. highly cited method [19] in the evaluation performed with the NIREP database [25]. The major drawback of Jacobi EPDiff PDE-LDDMM is the large memory load inherent to the Gauss–Newton–Krylov PDE-LDDMM formulation and aggravated by the large time-sampling needed for the stability of Runge–Kutta (RK) integration in the solution of the PDEs.

1.4. Our proposal

The purpose of this article is to propose three efficient variants of Jacobi EPDiff PDE-LDDMM methods with SL-RK integration and the band-limited parameterization. The analogs of the three variants have been previously proposed in [34,43] for PDE-LDDMM and gradient-descent optimization and recently extended to Newton–Krylov optimization in [39]. In this work, we provide the equations of the variants in the framework of Gauss–Newton–Krylov Jacobi EPDiff PDE-LDDMM and derive the involved PDEs in Semi-Lagrangian form in the spatial and the band-limited domains. Our proposal departs substantially from Jacobi EPDiff PDE-LDDMM [25] by:

- The completion of Jacobi EPDiff PDE-LDDMM with the best-performing PDE-LDDMM variants in [39].
- The derivation of the equations needed in the use of SL-RK solvers.
- The parameterization of the problem in the space of band-limited vector fields.

On the one hand, Jacobi EPDiff PDE-LDDMM [25] bridges the gap between Vialard et al. [19], Sing et al. [22], and Mang et al. [28] approaches for MCC PDE-LDDMM parameterized on the initial velocity field. On the other hand, the huge computational complexity of PDE-LDDMM has been substantially reduced using SL-RK integration and

the band-limited parameterization [38–40]. This work closes the loop among our previous works [25,38–40] by using SL-RK for PDE integration in Jacobi EPDiff PDE-LDDMM and formulating the problem in the space of band-limited vector fields.

Our best-performing method may be used in extensive studies for anatomical shape variability quantification [4], group wise comparison studies [16], and transversal and longitudinal population modeling [4, 22,44]. Our framework allows adding specific biophysical constraints to the variational problem. Therefore, these studies may be performed with physically plausible transformations, increasing the realism of the analysis. In addition, the derivation of the equations needed for the use of SL-RK solvers may be included in recently proposed deep-learning architectures for PDE-LDDMM and MCC PDE-LDDMM diffeomorphic registration (e.g. https://mermaid.readthedocs.io).

1.5. Manuscript organization

In the following, Section 2 describes the methodological background of LDDMM, MCC-LDDMM, PDE-LDDMM, and their band-limited versions. Section 3 presents our three proposed Jacobi EPDiff PDE-LDDMM methods in the spatial and band-limited domains. Section 4 presents the Semi-Lagrangian Runge–Kutta integration methods for the PDEs arising in Jacobi EPDiff PDE-LDDMM. Section 5 enumerates the most relevant implementation details. Section 6 shows the evaluation results conducted in this work. Finally, Section 7 gathers the most remarkable conclusions of our work.

2. Background on LDDMM methods

In this section, we briefly review the fundamental equations involved in the different families of LDDMM methods: original LDDMM proposed in Beg et al. [17], MCC-LDDMM proposed in Miller et al. and Younes et al. [20,21], and PDE-LDDMM proposed in Hart et al. [34] and extended in [39]. We provide the variational formulations and the fundamental equations for computing diffeomorphisms from the different tangent space parameterizations in the spatial and band-limited domains.

2.1. Spatial domain

Let $\Omega \subseteq \mathbb{R}^d$ be the image domain. Let $Diff(\Omega)$ be the LDDMM Riemannian manifold of diffeomorphisms and V the tangent space at the identity element. $Diff(\Omega)$ is a Lie group, and V is the corresponding Lie algebra. Let Δ be the Laplacian operator. The Riemannian metric of $Diff(\Omega)$ is defined from the scalar product in V, $\langle v, w\rangle_V = \langle Lv, w\rangle_{L^2}$, where $L = (Id - \alpha\Delta)^s, \alpha > 0, s \in \mathbb{N}$ is the invertible self-adjoint differential operator associated with the differential structure of $Diff(\Omega)$. We denote with K to the inverse of operator L. Let I_0 and I_1 be the source and the target images.

2.1.1. LDDMM

Large Deformation Diffeomorphic Metric Mapping [17] is formulated in the space of time-varying smooth flows of velocity fields in V from the minimization of the variational problem

$$E(v) = \frac{1}{2}\int_0^1 \langle Lv_t, v_t\rangle_{L^2} dt + \frac{1}{\sigma^2}\|I_0\circ(\phi_1^v)^{-1} - I_1\|^2_{L^2}. \tag{1}$$

Given $v_t \in L^2([0,1], V)$, the diffeomorphism $(\phi_1^v)^{-1}$ is defined as the solution at time $t = 1$ of the equation

$$\partial_t(\phi_t^v)^{-1} = -v_t\circ(\phi_t^v)^{-1} \tag{2}$$

with initial condition $(\phi_0^v)^{-1} = id$. The critical points of the length functional $\int_0^1 \|v_t\|_V dt$ are the critical points of the regularization energy since $\int_0^1 \langle Lv_t, v_t\rangle_{L^2} dt = \int_0^1 \|v_t\|^2_V dt$, and they are of constant speed. Under exact matching, a minimizer of Eq. (1) should verify that $\|I_0\circ(\phi_1^v)^{-1} - I_1\|^2_{L^2} = 0$ and then it should provide a geodesic path on $Diff(\Omega)$ [17,19]. In practice, the minimization of Eq. (1) can be seen as an approximation of the exact matching problem taking into account possible inaccuracies in the estimation of I_1 from $I_0\circ(\phi_1^v)^{-1}$ due to inherent differences between the images of different individuals. This means that the image similarity term cannot be zero at convergence, and, therefore, exact geodesics cannot be retrieved even after a large number of gradient descent iterations.

The LDDMM variational problem can be also set for steady velocity field flows [45], provided by the stationary parameterization of diffeomorphisms. In this case, the solutions do not belong to geodesic paths due to the right-invariance of the metric in $Diff(\Omega)$. We need the bi-invariance of the metric in order to have geodesics and one-parameter subgroups identified as one. However, this family of methods has become relevant due to their efficiency for applications where the $Diff(\Omega)$-metric minimizing property is not relevant for the clinical application.

2.1.2. MCC-LDDMM

Momentum conservation constrained LDDMM [21] is formulated in the space of initial velocity fields in V from the minimization of the energy functional

$$E(v_0) = \frac{1}{2}\langle Lv_0, v_0\rangle_{L^2} + \frac{1}{\sigma^2}\|I_0\circ(\phi_1^v)^{-1} - I_1\|^2_{L^2}, \tag{3}$$

where the time-varying flow v_t of $(\phi_1^v)^{-1}$ is computed from v_0 through geodesic shooting.

The MCC constraint has shown to be equivalent to the EPDiff equation [20,41]

$$\partial_t v_t + ad^\dagger_{v_t} v_t = 0 \text{ in } \Omega\times(0,1] \tag{4}$$

with initial condition v_0, where the operator $ad^\dagger_{v_t} w_t$ is the transpose of the adjoint operator

$$ad_{v_t} w_t = Dv_t\cdot w_t - Dw_t\cdot v_t, \tag{5}$$

yielding the extended expression of the EPDiff

$$\partial_t v_t + K[(Dv_t)^T\ Lv_t + DLv_t\ v_t + Lv_t\ \nabla\cdot v_t] = 0 \tag{6}$$

where D denotes the Jacobian matrix operator, and $\nabla\cdot$ the divergence. In this case, the solutions of the MCC-LDDMM problem verify the momentum conservation property and belong to geodesic paths.

2.1.3. PDE-LDDMM

PDE-constrained LDDMM [34] is formulated from the minimization of the variational problem

$$E(v) = \frac{1}{2}\int_0^1 \langle Lv_t, v_t\rangle_{L^2} dt + \frac{1}{\sigma^2}\|m(1) - I_1\|^2_{L^2}, \tag{7}$$

subject to the state equation

$$\partial_t m(t) + \nabla m(t)\cdot v_t = 0 \text{ in } \Omega\times(0,1], \tag{8}$$

with initial condition $m(0) = I_0$ [28,34], or subject to the deformation state equation

$$\partial_t\phi(t) + D\phi(t)\cdot v_t = 0 \text{ in } \Omega\times(0,1], \tag{9}$$

with initial condition $\phi(0) = id$ [39,43]. These problems can be formulated in the space of initial velocity fields in V or related magnitudes such as the scalar or vector momentum [19,22], where the EPDiff equation can be naturally added in the constraint set.

2.2. Band-limited domain

Let $\widetilde{\Omega} \subseteq \mathbb{C}^d$ be the discrete Fourier domain truncated with frequency bounds $K_1, \ldots, K_d$. We denote with $\widetilde{V}$ the space of discretized band-limited vector fields in V with these frequency bounds. The elements in

$\widetilde{V}$ are represented in the Fourier domain as $\tilde{v} : \widetilde{\Omega} \to \mathbb{C}^d$, $\tilde{v}(k_1, \dots, k_d)$, and in the spatial domain as $\imath(\tilde{v}) : \Omega \to \mathbb{R}^d$,

$$\imath(\tilde{v})(x_1, \dots, x_d) = \sum_{k_1=0}^{K_1} \cdots \sum_{k_d=0}^{K_d} \tilde{v}(k_1, \dots, k_d) e^{2\pi i k_1 x_1} \dots e^{2\pi i k_d x_d}. \tag{10}$$

The application $\imath : \widetilde{V} \to V$ denotes the natural inclusion mapping of $\widetilde{V}$ in V. The application $\pi : V \to \widetilde{V}$ denotes the projection of V onto $\widetilde{V}$.

$\widetilde{V}$ has a finite-dimensional Lie algebra structure using the truncated convolution in the definition of the Lie bracket [24]. We denote with $Diff(\widetilde{\Omega})$ to the finite-dimensional Riemannian manifold of diffeomorphisms on $\widetilde{\Omega}$ with corresponding Lie algebra $\widetilde{V}$. The Riemannian metric in $Diff(\widetilde{\Omega})$ is defined from the scalar product $\langle \tilde{v}, \tilde{w} \rangle_{\widetilde{V}} = \langle \tilde{L}\tilde{v}, \tilde{w} \rangle_{l^2}$, where $\tilde{L}$ denotes the projection of operator L in the truncated Fourier domain.

2.2.1. BL-LDDMM

Band-limited LDDMM [24] is formulated in the space of band-limited vector fields from the minimization of

$$E(\tilde{v}) = \frac{1}{2} \int_0^1 \langle \widetilde{L}\tilde{v}_t, \tilde{v}_t \rangle_{l^2} dt + \frac{1}{\sigma^2} \| I_0 \circ (\phi_1^v)^{-1} - I_1 \|_{L^2}^2, \tag{11}$$

where the diffeomorphism $(\phi_1^v)^{-1}$ is defined from the solution at time $t = 1$ of

$$\partial_t (\phi_t^v)^{-1} = -\imath(\tilde{v}_t) \circ (\phi_t^v)^{-1} \tag{12}$$

with initial condition $(\phi_0^v)^{-1} = id$.

2.2.2. MCC BL-LDDMM

The band-limited version of MCC LDDMM is formulated in the space of initial band-limited velocity fields in $\widetilde{V}$ from the minimization of the energy functional

$$E(\tilde{v}_0) = \frac{1}{2} \langle \widetilde{L}\tilde{v}_0, \tilde{v}_0 \rangle_{l^2} + \frac{1}{\sigma^2} \| I_0 \circ (\phi_1^v)^{-1} - I_1 \|_{L^2}^2, \tag{13}$$

subject to the projected EPDiff equation

$$\partial_t \tilde{v}_t + \widetilde{ad^\dagger_{\tilde{v}_t}} \tilde{v}_t = 0 \text{ in } \widetilde{\Omega} \times (0, 1], \tag{14}$$

where the expressions of the projection of operators ad and $ad^\dagger$ are given by

$$\widetilde{ad}_{\tilde{v}_t} \tilde{w}_t = \widetilde{D}\tilde{v}_t \star \tilde{w}_t - \widetilde{D}\tilde{w}_t \star \tilde{v}_t \tag{15}$$

$$\widetilde{ad^\dagger_{\tilde{v}_t}} \tilde{w}_t = \widetilde{K}[(\widetilde{D}\tilde{v}_t)^T \star \tilde{m}_t + \widetilde{D}\tilde{m}_t \star \tilde{v}_t + \tilde{m}_t \star \widetilde{\nabla \cdot} \tilde{v}_t], \tag{16}$$

where $\star$ denotes the truncated convolution operator.

2.2.3. BL PDE-LDDMM

The band-limited parameterization can be extended to PDE-LDDMM likewise LDDMM [38,39]. For BL PDE-LDDMM, the state and the deformation state equations are given by

$$\partial_t m(t) + \nabla m(t) \cdot \imath(v_t) = 0 \text{ in } \Omega \times (0, 1] \tag{17}$$

$$\partial_t \tilde{u}(t) + \widetilde{D}\tilde{u}(t) \star \tilde{v}_t = \tilde{v}_t \text{ in } \widetilde{\Omega} \times (0, 1], \tag{18}$$

where $\phi(t) = id - \imath(\tilde{u})$, i.e. $\tilde{u}$ represents the truncated Fourier transform of a displacement field.

3. Jacobi EPDiff PDE-constrained LDDMM

In this section, we present our three proposed variants of Jacobi EPDiff PDE-LDDMM methods. It should be noticed that the first variant in the spatial domain was previously proposed in [25] combined with Runge–Kutta integration. We start providing a complete description of the method since the second and the third variants and their band-limited versions are underpinned by this original method. As we will see in the experimental section, the BL version of the second and third variants combined with Semi-Lagrangian integration compete with this original first variant in terms of accuracy and greatly overpass it in terms of efficiency.

3.1. Jacobi EPDiff PDE-LDDMM based on the state equation (Variant I)

3.1.1. Problem statement in the spatial domain

Jacobi EPDiff PDE-LDDMM was originally proposed in [25]. The variational problem is given by the minimization of the energy functional

$$E(v_0) = \frac{1}{2} \langle L v_0, v_0 \rangle_{L^2} + \frac{1}{\sigma^2} \| m(1) - I_1 \|_{L^2}^2, \tag{19}$$

subject to the EPDiff and the state equation

$$\partial_t v_t + ad^\dagger_{v_t} v_t = 0 \text{ in } \Omega \times (0, 1] \tag{20}$$

$$\partial_t m(t) + \nabla m(t) \cdot v_t = 0 \text{ in } \Omega \times (0, 1], \tag{21}$$

with initial conditions $v(0) = v_0$ and $m(0) = I_0$, respectively.

Optimization is performed by combining the method of Lagrange multipliers with inexact Gauss–Newton–Krylov methods. The gradient and the Hessian is computed from the augmented Lagrangian [25]. The image similarity energy gradient is computed at $t = 1$ from

$$\nabla_{v_1} E_{\text{img}}(v_0) = K(\lambda(1) \cdot \nabla m(1)), \tag{22}$$

where the adjoint variable equals $\lambda(1) = -\frac{2}{\sigma^2}(m(1) - I_1)$. At this point, the gradient is integrated backward using the reduced adjoint Jacobi equations

$$\partial_t U_t + ad^\dagger_{v_t} U_t = 0 \text{ in } \Omega \times [0, 1) \tag{23}$$

$$\partial_t w_t - ad_{v_t} w_t + ad^\dagger_{w_t} v_t + U_t = 0 \text{ in } \Omega \times [0, 1) \tag{24}$$

with initial conditions $U(1) = \nabla_{v_1} E_{\text{img}}(v_0)$ and $w(1) = 0$ to obtain

$$\nabla_{v_0} E(v_0) = v_0 + w(0). \tag{25}$$

The second-order variations of the augmented Lagrangian yield the incremental EPDiff and incremental state equations, needed for the computation of the Hessian-vector product. Thus,

$$\partial_t \delta v_t + ad^\dagger_{\delta v_t} v_t + ad^\dagger_{v_t} \delta v_t = 0 \text{ in } \Omega \times (0, 1] \tag{26}$$

$$\partial_t \delta m(t) + \nabla \delta m(t) \cdot v_t + \nabla m(t) \cdot \delta v_t = 0 \text{ in } \Omega \times (0, 1] \tag{27}$$

with initial conditions $\delta v(0) = 0$ and $\delta m(0) = 0$. The Hessian-vector product $H_{v_0} E((v_0)\delta v_0$ is computed from the Hessian-vector product at $t = 1$ of the image similarity energy

$$H_{v_1} E_{\text{img}}(v_0)\delta v_0 = K(\delta\lambda(1) \cdot \nabla m(1)) + K(\lambda(1) \cdot \nabla \delta m(1)), \tag{28}$$

where $\delta\lambda(1) = -\frac{2}{\sigma^2}\delta m(1)$. Finally, $H_{v_1} E_{\text{img}}(v_0)\delta v_0$ is integrated backward using the reduced incremental adjoint Jacobi equations

$$\partial_t \delta U_t + ad^\dagger_{\delta v_t} U_t + ad^\dagger_{v_t} \delta U_t = 0 \text{ in } \Omega \times [0, 1) \tag{29}$$

$$\partial_t \delta w_t - ad_{\delta v_t} w_t - ad_{v_t} \delta w_t + ad^\dagger_{\delta w_t} v_t + ad^\dagger_{w_t} \delta v_t + \delta U_t = 0 \text{ in } \Omega \times [0, 1) \tag{30}$$

with initial conditions $\delta U(1) = H_{v_1} E_{\text{img}}(v_0)\delta v_0$ and $\delta w(1) = 0$ to obtain

$$H_{v_0} E(v_0)\delta v_0 = \delta v_0 + \delta w(0). \tag{31}$$

The Gauss–Newton approximation drops $K(\lambda(1) \cdot \nabla \delta m(1))$ from the expression of $H_{v_1} E_{\text{img}}$ and the ad_v and $ad^\dagger_w$ terms from the incremental adjoint Jacobi equation on δw, yielding a definite positive approximation. The minimization using a second-order inexact Gauss–Newton–Krylov method yields to the update equation

$$v_0^{n+1} = v_0^n + \epsilon \delta v_0^n, \tag{32}$$

where δv_0^n is computed from Conjugate Gradient on the system

$$H_{v_0} E(v_0^n)\delta {v_0}^n = -\nabla_{v_0} E(v_0^n). \tag{33}$$

The backward integration of the gradient and the Hessian using the Jacobi equations is the key feature of Jacobi EPDiff PDE-LDDMM methods. With them, we avoid the complex dependence on the initial

velocity field in the computations. We also avoid the numerical computation of the adjoint equation and its incremental counterpart that has been recently identified as a subtle problem in PDE-constrained LDDMM [30].

3.1.2. Problem statement in the band-limited domain

Band-Limited Jacobi EPDiff PDE-LDDMM is given by the minimization of the energy functional

$$E(\tilde{v}_0) = \frac{1}{2}\langle \tilde{L}\tilde{v}_0, \tilde{v}_0\rangle_{l^2} + \frac{1}{\sigma^2}\|m(1) - I_1\|^2_{L^2}, \tag{34}$$

subject to the band-limited EPDiff and the state equation

$$\partial_t \tilde{v}_t + \widetilde{ad^\dagger}_{\tilde{v}_t}\tilde{v}_t = 0 \text{ in } \widetilde{\Omega}\times(0,1] \tag{35}$$

$$\partial_t m(t) + \nabla m(t)\cdot \imath(\tilde{v}_t) = 0 \text{ in } \Omega\times(0,1], \tag{36}$$

with initial conditions $\tilde{v}(0) = \tilde{v}_0$ and $m(0) = I_0$, respectively. The image similarity energy gradient is computed at $t = 1$ from

$$\widetilde{\nabla}_{\tilde{v}_1} E_{\text{img}}(\tilde{v}_0) = \widetilde{K}(\pi(\lambda(1)\cdot\nabla m(1))), \tag{37}$$

which is integrated backward using the reduced band-limited adjoint Jacobi equations

$$\partial_t \tilde{U}_t + \widetilde{ad^\dagger}_{\tilde{v}_t}\tilde{U}_t = 0 \text{ in } \widetilde{\Omega}\times[0,1) \tag{38}$$

$$\partial_t \tilde{w}_t - \widetilde{ad}_{\tilde{v}_t}\tilde{w}_t + \widetilde{ad^\dagger}_{\tilde{w}_t}\tilde{v}_t + \tilde{U}_t = 0 \text{ in } \widetilde{\Omega}\times[0,1) \tag{39}$$

to obtain $\widetilde{\nabla}_{\tilde{v}_0} E(\tilde{v}_0) = \tilde{v}_0 + \tilde{w}(0)$.

The incremental band-limited EPDiff equation is given by

$$\partial_t \delta\tilde{v}_t + \widetilde{ad^\dagger}_{\delta\tilde{v}_t}\tilde{v}_t + \widetilde{ad^\dagger}_{\tilde{v}_t}\delta\tilde{v}_t = 0 \text{ in } \widetilde{\Omega}\times(0,1]. \tag{40}$$

The Gauss–Newton Hessian-vector product at $t = 1$ of the image similarity energy is given by

$$\widetilde{H}_{\tilde{v}_1} E_{\text{img}}(\tilde{v}_0)\delta\tilde{v}_0 = \widetilde{K}(\pi(\delta\lambda(1)\cdot\nabla m(1))), \tag{41}$$

which is integrated backward using the reduced incremental band-limited adjoint Jacobi equations

$$\partial_t \delta\tilde{U}_t + \widetilde{ad^\dagger}_{\delta\tilde{v}_t}\tilde{U}_t + \widetilde{ad^\dagger}_{\tilde{v}_t}\delta\tilde{U}_t = 0 \text{ in } \widetilde{\Omega}\times[0,1) \tag{42}$$

$$\partial_t \delta\tilde{w}_t - \widetilde{ad}_{\delta\tilde{v}_t}\tilde{w}_t + \widetilde{ad^\dagger}_{\delta\tilde{w}_t}\tilde{v}_t + \delta\tilde{U}_t = 0 \text{ in } \widetilde{\Omega}\times[0,1) \tag{43}$$

to obtain $\widetilde{H}_{\tilde{v}_0} E(\tilde{v}_0)\delta\tilde{v}_0 = \delta\tilde{v}_0 + \delta\tilde{w}(0)$.

The Gauss–Newton–Krylov update equation is given from

$$\tilde{v}_0^{n+1} = \tilde{v}_0^n + \epsilon\delta\tilde{v}_0^n, \tag{44}$$

where $\delta\tilde{v}_0^n$ is computed from Conjugate Gradient on the system

$$\widetilde{H}_{\tilde{v}_0} E(\tilde{v}_0^n)\delta\tilde{v}_0^n = -\widetilde{\nabla}_{\tilde{v}_0} E(\tilde{v}_0^n). \tag{45}$$

3.2. Alternative Jacobi EPDiff PDE-LDDMM based on the state equation (Variant II)

3.2.1. Problem statement in the spatial domain

The alternative version of Jacobi EPDiff PDE-LDDMM based on the state equation arises from the observation that the state variable m can be computed from

$$m(t) = I_0\circ\phi(t), \tag{46}$$

where $\phi(t)$ is computed from

$$\partial_t\phi(t) + D\phi(t)\cdot v_t = 0 \text{ in } \Omega\times(0,1], \tag{47}$$

with initial condition $\phi(0) = id$ in Ω [34]. With this approach, the expression of the gradient $\nabla_{v_1} E_{\text{img}}(v_0)$ is computed from Eq. (22), where the state variable is computed from Eqs. (46) and (47) rather than directly solving the state equation (Eq. (8)). The computation of the Hessian-vector product proceeds following Eqs. (28) to (31) where the incremental state variable δm is computed from

$$\delta m(t) = \nabla I_0\circ\phi(t)\cdot\delta\phi(t), \tag{48}$$

where $\delta\phi$ is computed from the first-order variation of Eq. (47)

$$\partial_t\delta\phi(t) + D\delta\phi(t)\cdot v_t + D\phi(t)\cdot\delta v(t) = 0 \text{ in } \Omega\times(0,1], \tag{49}$$

subject to $\delta\phi(0) = 0$.

3.2.2. Problem statement in the band-limited domain

In the band-limited version of the problem, the state equation is computed from $m(t) = I_0\circ\phi(t)$, where $\phi(t) = id - \imath(\tilde{u}(t))$ and $\tilde{u}$ is computed from the band-limited deformation state equation (Eq. (18)). Likewise, $\delta\tilde{m}(t) = \nabla I_0\circ\phi(t)\cdot\imath(\delta\tilde{u}(t))$.

3.3. Jacobi EPDiff PDE-LDDMM based on the deformation state equation (Variant III)

3.3.1. Problem statement in the spatial domain

Jacobi EPDiff PDE-LDDMM based on the deformation state equation is formulated from the minimization of Eq. (19) subject to the EPDiff and the deformation state equation

$$\partial_t v_t + ad^\dagger_{v_t} v_t = 0 \text{ in } \Omega\times(0,1] \tag{50}$$

$$\partial_t\phi(t) + D\phi(t)\cdot v_t = 0 \text{ in } \Omega\times(0,1], \tag{51}$$

with initial conditions $v(0) = v_0$ and $\phi(0) = id$, respectively.

For this PDE-constrained variational formulation, the image similarity energy gradient is computed at $t = 1$ from

$$\nabla_{v_1} E_{\text{img}}(v_0) = K(D\phi(1)\cdot\rho(1)), \tag{52}$$

where the adjoint variable $\rho(1) = -\frac{2}{\sigma^2}(m(1) - I_1)\cdot\nabla m(1)$. Then, $\nabla_{v_1} E_{\text{img}}(v_0)$ is integrated backward using the reduced adjoint Jacobi Eqs. (23) and (24) to obtain $\nabla_{v_0} E(v_0)$ similarly to original Jacobi EPDiff PDE-LDDMM.

The incremental EPDiff and the incremental state equation correspond with

$$\partial_t\delta v_t + ad^\dagger_{\delta v_t} v_t + ad^\dagger_{v_t}\delta v_t = 0 \text{ in } \Omega\times(0,1] \tag{53}$$

$$\partial_t\delta\phi(t) + D\delta\phi(t)\cdot v_t + D\phi(t)\cdot\delta v_t = 0 \text{ in } \Omega\times(0,1] \tag{54}$$

with initial conditions $\delta v(0) = 0$ and $\delta\phi(0) = 0$.

The Gauss–Newton approximation of the Hessian-vector product of the image similarity energy at $t = 1$ is given by

$$H_{v_1} E_{\text{img}}(v_0)\delta v_0 = K(D\phi(1)\delta\rho(1)), \tag{55}$$

where $\delta\rho(1)$ is approximated by $\delta\rho(1) \approx -\frac{2}{\sigma^2}\delta m(1)\cdot\nabla m(1)$. The expression $H_{v_1} E_{\text{img}}$ is integrated backward using the reduced incremental adjoint Jacobi Eqs. (29) and (30) to obtain the expression for $H_{v_0} E(v_0)\delta v_0$.

3.3.2. Problem statement in the band-limited domain

The band-limited version of Jacobi EPDiff PDE-LDDMM based on the deformation state equation is formulated from the minimization of Eq. (34) subject to the band-limited EPDiff and deformation state equations (Eqs. (18) and (35), respectively). The image similarity energy gradient is computed at $t = 1$ from

$$\widetilde{\nabla}_{\tilde{v}_1} E_{\text{img}}(\tilde{v}_0) = \widetilde{K}(\widetilde{D}\tilde{u}(1)\star\tilde{\rho}(1)), \tag{56}$$

where the adjoint variable $\tilde{\rho}(1) = \pi(-\frac{2}{\sigma^2}(m(1) - I_1)\cdot\nabla m(1))$. The gradient $\widetilde{\nabla}_{\tilde{v}_1} E_{\text{img}}(\tilde{v}_0)$ is integrated backward using the reduced band-limited adjoint Jacobi Eqs. (38) and (39) to obtain $\widetilde{\nabla}_{\tilde{v}_0} E(\tilde{v}_0)$ similarly to the

band-limited versions of Jacobi EPDiff PDE-LDDMM based on the state equation.

The Gauss–Newton approximation of the Hessian-vector product of the image similarity energy at $t = 1$ is given by

$$\widetilde{H}_{\tilde{v}_1} E_{\text{img}}(\tilde{v}_0)\delta\tilde{v}_0 = \widetilde{K}(\widetilde{D}\tilde{u}(1) \star \delta\tilde{\rho}(1)), \tag{57}$$

where $\delta\tilde{\rho}(1) \approx \pi(-\frac{2}{\sigma^2}\delta m(1)\cdot\nabla m(1))$. The expression $\widetilde{H}_{\tilde{v}_1} E_{\text{img}}$ is integrated backward using the reduced band-limited incremental adjoint Jacobi Eqs. (42) and (43) to obtain the expression for $\widetilde{H}_{\tilde{v}_0} E(\tilde{v}_0)\delta\tilde{v}_0$.

3.4. General algorithms

Algorithm 1 presents the pseudocode for the spatial versions of Variants I and II. Algorithm 2 presents the pseudocode for Variant III. The pseudocode of the spatial versions of the three variants shares the steps for obtaining $\nabla_{v_0} E_{\text{img}}(v_0)$ from $\nabla_{v_1} E_{\text{img}}(v_0)$ and $H_{v_0} E_{\text{img}}(v_0)\delta v_0$ from $H_{v_1} E_{\text{img}}(v_0)\delta v_0$. The computation of the gradient and the Hessian at the $t = 1$ can be computed similarly to [39,40] by adding the computations of v_t and δv_t from the EPDiff and the incremental EPDiff equations. The algorithms of the BL versions can be written analogously taking into account the computations in the truncated Fourier domain with the equations provided below in this section.

Algorithm 1. Jacobi EPDiff PDE-LDDMM. Variants I and II.

Data: I_0, I_1, $v^0 \in V$, L, σ, ϵ, PCG_its.
Results: $v_0 \in V$, $m(1)$ solutions of Eq. (19) subject to the EPDiff and the state equation or $m(t) = I_0 \circ \phi(t)$ from the deformation state equation.
for $n \leftarrow 0$ **to** convergence **do**
1) Compute $v^{n+1}(t)$ forward in time from Eq. (20) and $v(0) = v_0^n$.
2) Compute $m^{n+1}(1)$ forward in time from Eq. (21) and $m(0) = I_0$ (Variant I) or $m(1) = I_0 \circ \phi(1)$ (Variant II).
3) Compute $\lambda^{n+1}(1) = -\frac{2}{\sigma^2}(m^{n+1}(1) - I_1)$.
4) Compute $\nabla_{v_1} E_{\text{img}}(v_0)^{n+1}$ from Eq. (22).
5) Compute $U^{n+1}(t)$ backward in time from Eq. (23) and $U(1) = \nabla_{v_1} E_{\text{img}}(v_0)^{n+1}$.
6) Compute $w^{n+1}(t)$ backward in time from Eq. (24) and $w(1) = 0$.
7) Compute $\nabla_{v_0} E_{\text{img}}(v_0)^{n+1}$ from Eq. (25).
8) Compute δv_0^{n+1} from Eq. (33).
for $k \leftarrow 0$ **to** PCG convergence or PCG_its **do**
8.1) Compute $\delta v^{k+1}(t)$ forward in time from Eq. (26) and $\delta v(0) = 0$.
8.2) Compute $\delta m^{k+1}(1)$ forward in time from Eq. (27) and $\delta m(0) = 0$ (Variant I) or Eq. (48) (Variant II).
8.3) Compute $\delta\lambda^{k+1}(1) = -\frac{2}{\sigma^2}\delta m^{k+1}(1)$.
8.4) Compute $(H_{v_1} E_{\text{img}}(v_0)\delta v_0)^{k+1}$ from Eq. (28).
8.5) Compute $\delta U^{k+1}(t)$ backward in time from Eq. (29) and $\delta U(1) = (H_{v_1} E_{\text{img}}(v_0)\delta v_0)^{k+1}$.
8.6) Compute $\delta w^{k+1}(t)$ backward in time from Eq. (30) and $\delta w(1) = 0$.
8.7) Compute $(H_{v_0} E_{\text{img}}(v_0)\delta v_0)^{k+1}$ from Eq. (31).
8.8) Compute δv_0^{k+1} from PCG at iteration $k + 1$.
8.9) Check PCG convergence.
end
9) Compute v_0^{n+1} from Eq. (32).
10) Check algorithm convergence.
end

Algorithm 2. Jacobi EPDiff PDE-LDDMM. Variant III.

Data: I_0, I_1, $v^0 \in V$, L, σ, ϵ, PCG_its.
Results: $v_0 \in V$, $m(1)$ solutions of Eq. (19) subject to the EPDiff and the deformation state equation.
for $n \leftarrow 0$ **to** convergence **do**
1) Compute $v^{n+1}(t)$ forward in time from Eq. (50) and $v(0) = v_0^n$.
2) Compute $\phi^{n+1}(t)$ forward in time from Eq. (51) and $\phi(0) = id$.
3) Compute $m^{n+1}(1)$ from $m(t) = I_0 \circ \phi(t)$.
3) Compute $\rho^{n+1}(1) = -\frac{2}{\sigma^2}(m^{n+1}(1) - I_1)\cdot\nabla m(1)$.
4) Compute $\nabla_{v_1} E_{\text{img}}(v_0)^{n+1}$ from Eq. (52).
5) Compute $U^{n+1}(t)$ backward in time from Eq. (23) and $U(1) = \nabla_{v_1} E_{\text{img}}(v_0)^{n+1}$.
6) Compute $w^{n+1}(t)$ backward in time from Eq. (24) and $w(1) = 0$.
7) Compute $\nabla_{v_0} E_{\text{img}}(v_0)^{n+1}$ from Eq. (25).
8) Compute δv_0^{n+1} from Eq. (33).
for $k \leftarrow 0$ **to** PCG convergence or PCG_its **do**
8.1) Compute $\delta v^{k+1}(t)$ forward in time from Eq. (53) and $\delta v(0) = 0$.
8.2) Compute $\delta\phi^{k+1}(t)$ forward in time from Eq. (54) and $\delta\phi(0) = 0$.
8.3) Compute $\delta\rho^{k+1}(1) = -\frac{2}{\sigma^2}\delta m^{k+1}(1)\cdot\nabla m^{k+1}(1)$.
8.4) Compute $(H_{v_1} E_{\text{img}}(v_0)\delta v_0)^{k+1}$ from Eq. (28).
8.5) Compute $\delta U^{k+1}(t)$ backward in time from Eq. (29) and $\delta U(1) = (H_{v_1} E_{\text{img}}(v_0)\delta v_0)^{k+1}$.
8.6) Compute $\delta w^{k+1}(t)$ backward in time from Eq. (30) and $\delta w(1) = 0$.
8.7) Compute $(H_{v_0} E_{\text{img}}(v_0)\delta v_0)^{k+1}$ from Eq. (31).
8.8) Compute δv_0^{k+1} from PCG at iteration $k + 1$.
8.9) Check PCG convergence.
end
9) Compute v_0^{n+1} from Eq. (32).
10) Check algorithm convergence.
end

4. Semi-Lagrangian Runge–Kutta PDE integration

4.1. Semi-Lagrangian Runge–Kutta methods in the spatial domain

Semi-Lagrangian (SL) integration methods allow solving the transport equations of the general form

$$D_t u = f(u, v), \tag{58}$$

where $u : \Omega \times [0, 1] \to \mathbb{R}^d$ is a scalar or a vector function varying in time, and

$$D_t u = \partial_t u + Du \cdot v. \tag{59}$$

SL methods combine the most relevant properties of Eulerian and Lagrangian schemes. On the one hand, SL methods involve following the characteristic lines of the differential equation, in a similar way to Lagrangian approaches. On the other hand, the equation is solved on the regular grid, like Eulerian approaches. As a result, SL methods are unconditionally stable as the Lagrangian schemes. This means that time sampling can be selected according to accuracy considerations rather than stability considerations. SL methods allow selecting a time sampling usually much smaller than Eulerian methods yielding a sensible reduction of the computational complexity.

SL schemes involve two steps. First, the departure points are computed solving the characteristic equation

$$D_t X(t) = v(t, X(t)), \tag{60}$$

with initial condition $X(0) = x$. The direction of the time integration can be forward or backward, depending on the direction of the time

Table 1
Original PDEs involved in the different variants of Jacobi EPDiff PDE-LDDMM and corresponding PDEs written in SL form.

Equation in original form	Equation in SL form
$\partial_t v_t + ad^{\dagger}_{v_t} v_t = 0$	n.a.
$\partial_t \delta v_t + ad^{\dagger}_{\delta v_t} v_t + ad^{\dagger}_{v_t} \delta v_t = 0$	$D_t \delta v_t = -ad^{\dagger}_{\delta v_t} v_t - K((Dv_t)^T L \delta v_t + L \delta v_t \nabla \cdot v_t)$
$\partial_t m(t) + \nabla m(t) \cdot v_t = 0$	$D_t m(t) = 0$
$\partial_t \delta m(t) + \nabla \delta m(t) \cdot v_t + \nabla m(t) \cdot \delta v_t = 0$	$D_t \delta m(t) = -\nabla m(t) \cdot \delta v_t$
$\partial_t \phi(t) + D\phi(t) \cdot v_t = 0$	$D_t \phi(t) = 0$
$\partial_t \delta\phi(t) + D\delta\phi(t) \cdot v_t + D\phi(t) \cdot \delta v_t = 0$	$D_t \delta\phi(t) = -D\phi(t) \cdot \delta v_t$
$\partial_t U_t + ad^{\dagger}_{v_t} U_t = 0$	$D_t U_t = -K((Dv_t)^T L U_t + L U_t \nabla \cdot v_t)$
$\partial_t w_t - ad_{v_t} w_t + ad^{\dagger}_{w_t} v_t + U_t = 0$	$D_t w_t = Dv_t w_t - ad^{\dagger}_{w_t} v_t - U_t$
$\partial_t \delta U_t + ad^{\dagger}_{\delta v_t} U_t + ad^{\dagger}_{v_t} \delta U_t = 0$	$D_t \delta U_t = -K((Dv_t)^T L \delta U_t + L \delta U_t \nabla \cdot v_t) - ad^{\dagger}_{\delta v_t} U_t$
$\partial_t \delta w_t - ad_{v_t} \delta w_t + ad^{\dagger}_{\delta w_t} v_t + \delta U_t = 0$	$D_t \delta w_t = Dv_t \delta w_t - ad^{\dagger}_{\delta w_t} v_t - \delta U_t$

integration of the transport equation. From the several methods proposed in the literature for solving the characteristic equation, we use the approach given by Mang and Biros in [35]

$$X_* = x - \delta t \cdot v, \tag{61}$$

$$v_* = v \circ X_*, \tag{62}$$

$$X_* = x - 0.5\ \delta t \cdot (v_* + v). \tag{63}$$

Second, the transport equation (Eq. (58)) is solved in the Eulerian grid

$$D_t u(X(t), t) = f(u(X(t), t), v(t, X(t))) \tag{64}$$

along the characteristic line X. The use of Runge–Kutta (RK) integration has been recently proposed in this step, yielding a higher-order accurate Semi-Lagrangian Runge–Kutta (SL-RK) method [46].

To be able to apply SL or SL-RK integration, the differential equations need to be written in the shape of Eq. (64). For SL-RK integration, the resulting right-hand side expression can be directly plugged into an RK differential solver. The derivation of the equations needed in Jacobi EPDiff PDE-LDDMM in SL form use the terms of the expansion of the EPDiff equation and the adjoint action (see the derivation in the Appendix). Table 1 gathers the expressions of the resulting differential equations. It should be noticed that the EPDiff equation computes the velocity field v needed to solve the characteristic equation. Therefore, it cannot be solved using SL-RK schemes. We used a RK scheme similarly to [25].

Table 2
Original PDEs involved in the different variants of BL Jacobi EPDiff PDE-LDDMM and corresponding PDEs written in SL form.

Equation in original form	Equation in SL form
$\partial_t \tilde{v}_t + \widetilde{ad}^{\dagger}_{\tilde{v}_t} \tilde{v}_t = 0$	n.a.
$\partial_t \delta\tilde{v}_t + \widetilde{ad}^{\dagger}_{\delta\tilde{v}_t} \tilde{v}_t + \widetilde{ad}^{\dagger}_{\tilde{v}_t} \delta\tilde{v}_t = 0$	$\widetilde{D}_t \delta\tilde{v}_t = -\widetilde{ad}^{\dagger}_{\delta\tilde{v}_t} \tilde{v}_t - \widetilde{K}((\widetilde{D}\tilde{v}_t)^T \star \widetilde{L}\delta\tilde{v}_t + \widetilde{L}\delta\tilde{v}_t \star \widetilde{\nabla}\cdot\tilde{v}_t)$
$\partial_t m(t) + \nabla m(t) \cdot \imath(\tilde{v}_t) = 0$	$D_t m(t) = 0$
$\partial_t \delta m(t) + \nabla \delta m(t) \cdot \imath(\tilde{v}_t) + \nabla m(t) \cdot \imath(\delta\tilde{v}_t) = 0$	$D_t \delta m(t) = -\nabla m(t) \cdot \imath(\delta\tilde{v}_t)$
$\partial_t \tilde{u}(t) + \widetilde{D}\tilde{u}(t) \star \tilde{v}_t = \tilde{v}_t$	$\widetilde{D}_t \tilde{u}(t) = \tilde{v}_t$
$\partial_t \delta\tilde{u}(t) + \widetilde{D}\delta\tilde{u}(t) \star \tilde{v}_t + \widetilde{D}\tilde{u}(t) \star \delta\tilde{v}_t = \delta\tilde{v}_t$	$\widetilde{D}_t \delta\tilde{u}(t) = \delta\tilde{v}_t - \widetilde{D}\tilde{u}(t) \star \delta\tilde{v}_t$
$\partial_t \tilde{U}_t + \widetilde{ad}^{\dagger}_{\tilde{v}_t} \tilde{U}_t = 0$	$\widetilde{D}_t \tilde{U}_t = -\widetilde{K}((\widetilde{D}\tilde{v}_t)^T \star \widetilde{L}\tilde{U}_t + \widetilde{L}\tilde{U}_t \star \widetilde{\nabla}\cdot\tilde{v}_t)$
$\partial_t \imath\tilde{w}_t - \widetilde{ad}_{\tilde{v}_t} \imath\tilde{w}_t + \widetilde{ad}^{\dagger}_{\imath\tilde{w}_t} \tilde{v}_t + \tilde{U}_t = 0$	$\widetilde{D}_t \imath\tilde{w}_t = \widetilde{D}\tilde{v}_t \star \imath\tilde{w}_t - \widetilde{ad}^{\dagger}_{\imath\tilde{w}_t} \tilde{v}_t - \tilde{U}_t$
$\partial_t \delta\tilde{U}_t + \widetilde{ad}^{\dagger}_{\delta\tilde{v}_t} \tilde{U}_t + \widetilde{ad}^{\dagger}_{\tilde{v}_t} \delta\tilde{U}_t = 0$	$\widetilde{D}_t \delta\tilde{U}_t = -\widetilde{K}((\widetilde{D}\tilde{v}_t)^T \star \widetilde{L}\delta\tilde{U}_t + \widetilde{L}\delta\tilde{U}_t \star \widetilde{\nabla}\cdot\tilde{v}_t) - \widetilde{ad}^{\dagger}_{\delta\tilde{v}_t} \tilde{U}_t$
$\partial_t \delta\imath\tilde{w}_t - \widetilde{ad}_{\tilde{v}_t} \delta\imath\tilde{w}_t + \widetilde{ad}^{\dagger}_{\delta\imath\tilde{w}_t} \tilde{v}_t + \delta\tilde{U}_t = 0$	$\widetilde{D}_t \delta\imath\tilde{w}_t = \widetilde{D}\tilde{v}_t \star \delta\imath\tilde{w}_t - \widetilde{ad}^{\dagger}_{\delta\imath\tilde{w}_t} \tilde{v}_t - \delta\tilde{U}_t$

Table 3
List of the PDE-LDDMM methods compared in this work. The table gathers the name of the methods used in the experimental section, the variant identifier, the integration scheme, and the publication where the method first appeared for the spatial (SP) and the band-limited (BL) parameterization. In the table, St. stands for stationary, NSt. for non-stationary, and J. for Jacobi. PDE-LDDMM refers to the original variant based on the state equation (Variant I), PDE-LDDMM st. eq. refers to the alternative variant based on the state equation (Variant II), and PDE-LDDMM def. st. eq. refers to the variant based on the deformation state equation (Variant III). It should be noticed that the works of Hart et al. and Polzin et al. use different approaches for integration and optimization. They are added to the table since they inspired the later Gauss–Newton–Krylov versions with RK integration.

Method	Variant	Integration	Publication (SP)	Publication (BL)
St. PDE-LDDMM	I	RK	Mang et al. [28]	Hernandez [38]
St. PDE-LDDMM st. eq.	II	RK	Hernandez [39]	Hernandez [39]
St. PDE-LDDMM def. st. eq.	III	RK	Hernandez [39]	Hernandez [39]
St. PDE-LDDMM	I	SL-RK	Mang et al. [35]	Hernandez [40]
St. PDE-LDDMM st. eq.	II	SL-RK	Hernandez [40]	Hernandez [40]
St. PDE-LDDMM def. st. eq.	III	SL-RK	Hernandez [40]	Hernandez [40]
NSt. PDE-LDDMM	I	RK	Hart et al. Mang et al. [28,34]	Hernandez [38]
NSt. PDE-LDDMM, st. eq.	II	RK	Hart et al. Hernandez [34,39]	Hernandez [39]
NSt. PDE-LDDMM, def. st. eq.	III	RK	Polzin et al. Hernandez [39,43]	Hernandez [39]
NSt. PDE-LDDMM	I	SL-RK	Hernandez [40]	Hernandez [40]
NSt. PDE-LDDMM st. eq.	II	SL-RK	Hernandez [40]	Hernandez [40]
NSt. PDE-LDDMM def. st. eq.	III	SL-RK	Hernandez [40]	Hernandez [40]
J. EPDiff PDE-LDDMM	I	RK	Hernandez [25]	this work
J. EPDiff PDE-LDDMM, st, eq.	II	RK	this work	this work
J. EPDiff PDE-LDDMM, def. st. eq.	III	RK	this work	this work
J. EPDiff PDE-LDDMM	I	SL-RK	this work	this work
J. EPDiff PDE-LDDMM, st. eq.	II	SL-RK	this work	this work
J. EPDiff PDE-LDDMM, def. st. eq.	III	SL-RK	this work	this work

Table 4
Mean and standard deviation of the relative image similarity error MSE_{rel} given in %, the relative gradient magnitude $\|g\|_{\infty,rel}$, and the minimum and maximum of the Jacobian determinant associated with the transformation $\phi(1)$. For each method, the value of the time sampling n_t is shown. For the SL-RK methods, the value of n_t for the solution of the EPDiff equation with RK integration is 30 for the spatial methods and 25 for the BL ones. Boldface highlights the best MSE_{rel} values for each group of variants. FL stands for Flux Limiter. (*) The n_t selected for NSt. PDE-LDDMM, st. eq. with RK integration was due to a memory load greater than the GPU maximum capacity (24 GBS).

Method	Variant	Integration	n_t	$MSE_{rel}(\%)$	$\|g\|_{\infty,rel}$	$\min(J(\phi(1)))$	$\max(J(\phi(1)))$
Vialard et al. IJCV 2011	–	FL	10	37.91 ± 2.40	0.29 ± 0.05	0.27 ± 0.23	1.63 ± 0.15
Singh et al. ISBI 2013	–	RK	30	21.97 ± 4.14	0.15 ± 0.08	0.14 ± 0.07	3.18 ± 0.95
Yang et al. MICCAI 2015	–	RK	30	**20.86 ± 2.36**	0.14 ± 0.10	0.12 ± 0.04	3.02 ± 0.69
SP Zhang et al. IJCV 2018	–	RK	30	20.92 ± 2.05	0.04 ± 0.02	0.20 ± 0.03	2.57 ± 0.29
St. PDE-LDDMM	I	RK	50	18.29 ± 2.83	0.07 ± 0.05	0.16 ± 0.05	3.70 ± 0.51
St. PDE-LDDMM st. eq.	II	RK	30	18.42 ± 2.71	0.18 ± 0.19	0.07 ± 0.06	2.95 ± 0.41
St. PDE-LDDMM def. st. eq.	III	RK	30	**16.83 ± 1.53**	0.16 ± 0.08	0.12 ± 0.05	4.12 ± 1.41
St. PDE-LDDMM	I	SL-RK	5	19.55 ± 1.76	0.14 ± 0.13	0.03 ± 0.04	3.25 ± 0.29
St. PDE-LDDMM st. eq.	II	SL-RK	5	18.34 ± 1.68	0.23 ± 0.21	0.03 ± 0.04	3.46 ± 0.69
St. PDE-LDDMM def. st. eq.	III	SL-RK	5	**17.10 ± 1.50**	0.12 ± 0.05	0.14 ± 0.05	5.02 ± 1.01
NSt. PDE-LDDMM	I	RK	50	22.68 ± 5.49	0.26 ± 0.12	0.16 ± 0.05	3.38 ± 0.90
NSt. PDE-LDDMM, st. eq.	II	RK	25*	29.92 ± 2.41	0.32 ± 0.10	0.11 ± 0.07	2.93 ± 0.78
NSt. PDE-LDDMM, def. st. eq.	II	RK	30	**16.10 ± 1.70**	0.20 ± 0.08	0.09 ± 0.03	4.55 ± 0.69
NSt. PDE-LDDMM	I	SL-RK	5	22.44 ± 6.26	0.51 ± 0.18	0.02 ± 0.02	3.96 ± 0.65
NSt. PDE-LDDMM st. eq.	II	SL-RK	5	21.82 ± 2.51	0.49 ± 0.19	0.01 ± 0.02	4.20 ± 0.94
NSt. PDE-LDDMM def. st. eq.	III	SL-RK	5	**16.86 ± 1.91**	0.13 ± 0.04	0.09 ± 0.02	7.35 ± 2.63
J. EPDiff PDE-LDDMM	I	RK	30	19.45 ± 2.39	0.16 ± 0.09	0.10 ± 0.05	3.09 ± 0.85
J. EPDiff PDE-LDDMM, st. eq.	II	RK	30	**18.46 ± 2.29**	0.15 ± 0.13	0.10 ± 0.06	3.15 ± 1.01
J. EPDiff PDE-LDDMM, def. st. eq.	III	RK	30	21.26 ± 3.38	0.23 ± 0.08	0.13 ± 0.05	2.47 ± 0.40
J. EPDiff PDE-LDDMM	I	SL-RK	5	27.97 ± 2.43	0.68 ± 0.40	0.21 ± 0.07	2.91 ± 0.61
J. EPDiff PDE-LDDMM, st. eq.	II	SL-RK	5	**16.52 ± 2.49**	0.25 ± 0.17	0.11 ± 0.05	5.28 ± 1.52
J. EPDiff PDE-LDDMM, def. st. eq.	III	SL-RK	5	18.21 ± 2.52	0.28 ± 0.17	0.13 ± 0.06	4.57 ± 1.32
BL Zhang et al. IJCV 2018 32x	–	RK	25	21.28 ± 2.07	0.01 ± 0.00	0.14 ± 0.02	2.51 ± 0.19
BL Zhang et al. IJCV 2018 40x	–	RK	25	20.84 ± 2.03	0.01 ± 0.00	0.14 ± 0.02	2.51 ± 0.19
BL Zhang et al. IJCV 2018 64x	–	RK	25	**20.56 ± 2.00**	0.01 ± 0.00	0.13 ± 0.03	2.52 ± 0.17
BL St. PDE-LDDMM 40x	I	RK	25	20.99 ± 2.59	0.04 ± 0.03	0.21 ± 0.04	3.32 ± 0.41
BL St. PDE-LDDMM st. eq. 32x	II	RK	25	18.53 ± 1.71	0.02 ± 0.01	0.11 ± 0.07	3.10 ± 0.35
BL St. PDE-LDDMM def. st. eq. 32x	III	RK	25	**17.32 ± 1.68**	0.03 ± 0.01	0.13 ± 0.05	3.76 ± 0.49
BL St. PDE-LDDMM 40x	I	SL-RK	5	20.41 ± 1.89	0.02 ± 0.00	0.32 ± 0.02	9.65 ± 4.77
BL St. PDE-LDDMM st. eq. 32x	II	SL-RK	5	19.89 ± 1.76	0.01 ± 0.00	0.29 ± 0.03	7.94 ± 2.81
BL St. PDE-LDDMM def. st. eq. 32x	III	SL-RK	5	**17.77 ± 1.66**	0.04 ± 0.01	0.21 ± 0.03	8.23 ± 3.24
BL NSt. PDE-LDDMM 40x	I	RK	25	29.30 ± 3.50	0.21 ± 0.08	0.24 ± 0.05	2.25 ± 0.51
BL NSt. PDE-LDDMM, st. eq. 32x	II	RK	25	29.21 ± 3.96	0.24 ± 0.11	0.15 ± 0.06	2.71 ± 0.48
BL NSt. PDE-LDDMM, def. st. eq. 32x	III	RK	25	**15.68 ± 1.52**	0.04 ± 0.01	0.09 ± 0.04	4.77 ± 0.78
BL NSt. PDE-LDDMM 40x	I	SL-RK	5	19.14 ± 2.06	0.11 ± 0.05	0.01 ± 0.07	5.25 ± 0.80
BL NSt. PDE-LDDMM st. eq. 32x	II	SL-RK	5	20.49 ± 1.75	0.17 ± 0.15	0.07 ± 0.03	4.51 ± 0.61
BL NSt. PDE-LDDMM def. st. eq. 32x	III	SL-RK	5	**16.80 ± 1.57**	0.07 ± 0.03	0.09 ± 0.03	7.37 ± 1.43
BL J. EPDiff PDE-LDDMM 32x	I	RK	25	26.95 ± 2.52	0.15 ± 0.07	0.23 ± 0.05	2.60 ± 0.70
BL J. EPDiff PDE-LDDMM, st. eq. 32x	II	RK	25	**19.55 ± 1.85**	0.09 ± 0.03	0.12 ± 0.06	3.40 ± 0.73
BL J. EPDiff PDE-LDDMM, def. st. eq. 32x	III	RK	25	22.56 ± 2.94	0.09 ± 0.03	0.17 ± 0.05	2.64 ± 0.36
BL J. EPDiff PDE-LDDMM 40x	I	RK	25	26.97 ± 3.07	0.15 ± 0.08	0.23 ± 0.05	2.61 ± 0.88
BL J. EPDiff PDE-LDDMM, st. eq. 40x	II	RK	25	**19.17 ± 2.19**	0.09 ± 0.04	0.13 ± 0.05	3.35 ± 0.46
BL J. EPDiff PDE-LDDMM, def. st. eq. 40x	III	RK	25	22.43 ± 3.00	0.08 ± 0.03	0.17 ± 0.05	2.57 ± 0.40
BL J. EPDiff PDE-LDDMM 64x	I	RK	25	26.52 ± 2.94	0.14 ± 0.07	0.23 ± 0.05	2.41 ± 0.38
BL J. EPDiff PDE-LDDMM, st. eq. 64x	II	RK	25	**19.59 ± 2.41**	0.09 ± 0.06	0.14 ± 0.05	3.10 ± 0.63
BL J. EPDiff PDE-LDDMM, def. st. eq. 64x	III	RK	25	22.27 ± 3.05	0.08 ± 0.03	0.16 ± 0.04	2.50 ± 0.40
BL J. EPDiff PDE-LDDMM 32x	I	SL-RK	5	25.45 ± 2.16	0.10 ± 0.04	0.25 ± 0.05	5.30 ± 1.26
BL J. EPDiff PDE-LDDMM, st. eq. 32x	II	SL-RK	5	**17.55 ± 1.83**	0.08 ± 0.03	0.18 ± 0.05	14.54 ± 11.69
BL J. EPDiff PDE-LDDMM, def. st. eq. 32x	III	SL-RK	5	19.46 ± 2.61	0.13 ± 0.15	0.20 ± 0.06	9.77 ± 5.43
BL J. EPDiff PDE-LDDMM 40x	I	SL-RK	5	25.25 ± 2.21	0.10 ± 0.03	0.25 ± 0.05	5.47 ± 1.67
BL J. EPDiff PDE-LDDMM, st. eq. 40x	II	SL-RK	5	**17.01 ± 1.87**	0.09 ± 0.04	0.19 ± 0.05	12.90 ± 9.79
BL J. EPDiff PDE-LDDMM, def. st. eq. 40x	III	SL-RK	5	18.76 ± 2.82	0.09 ± 0.03	0.20 ± 0.06	8.98 ± 4.14
BL J. EPDiff PDE-LDDMM 64x	I	SL-RK	5	25.25 ± 2.50	0.11 ± 0.04	0.25 ± 0.06	5.06 ± 1.23
BL J. EPDiff PDE-LDDMM, st. eq. 64x	II	SL-RK	5	**16.65 ± 2.11**	0.11 ± 0.06	0.18 ± 0.07	11.34 ± 6.11
BL J. EPDiff PDE-LDDMM, def. st. eq. 64x	III	SL-RK	5	18.45 ± 2.83	0.12 ± 0.06	0.19 ± 0.06	7.92 ± 2.28

4.2. Semi-Lagrangian Runge–Kutta methods in the band-limited domain

Semi-Lagrangian integration also allows solving band-limited transport equations of the general form

$$\widetilde{D}_t \tilde{u} = \tilde{f}(\tilde{u}, \tilde{v}), \tag{65}$$

where $\tilde{u} : \widetilde{\Omega} \times [0,1] \to \mathbb{C}^d$ is a time-varying scalar or vector function defined in the band-limited domain, and

$$\widetilde{D}_t \tilde{u} = \partial_t \tilde{u} + \widetilde{D}\tilde{u} \star \tilde{v}. \tag{66}$$

In this case, the departure points are computed solving the characteristic equation

$$D_t X(t) = \iota(\tilde{v}(t, \tilde{X}(t))), \tag{67}$$

Table 5
Computational complexity. GPU peak memory usage and mean and standard deviation of the computation time. Experiments run in an NVidia Titan RTX with 24 GBS of video memory.

Method	Integration	VRAM (MBS)	total time (s)
Singh et al. ISBI 2013	RK	13333	877.97 ± 252.20
Yang et al. MICCAI 2015	RK	16423	1945.99 ± 261.55
SP Zhang et al. IJCV 2018	RK	9641	1215.45 ± 179.07
St. PDE-LDDMM	RK	10311	2281.40 ± 378.56
St. PDE-LDDMM st. eq.	RK	17229	877.85 ± 176.03
St. PDE-LDDMM def. st. eq.	RK	15321	1298.50 ± 151.19
St. PDE-LDDMM	SL-RK	3901	118.29 ± 4.77
St. PDE-LDDMM st. eq.	SL-RK	6267	139.91 ± 22.06
St. PDE-LDDMM def. st. eq.	SL-RK	5935	221.01 ± 2.40
NSt. PDE-LDDMM	RK	14913	3443.17 ± 932.45
NSt. PDE-LDDMM, st. eq.	RK	20635	816.79 ± 480.61
NSt. PDE-LDDMM, def. st. eq.	RK	19065	2222.04 ± 369.96
NSt. PDE-LDDMM	SL-RK	11155	191.96 ± 45.53
NSt. PDE-LDDMM st. eq.	SL-RK	12429	214.09 ± 48.54
NSt. PDE-LDDMM def. st. eq.	SL-RK	12065	355.47 ± 4.38
J. EPDiff PDE-LDDMM	RK	14603	2590.56 ± 489.39
J. EPDiff PDE-LDDMM, st. eq.	RK	18027	2766.46 ± 609.31
J. EPDiff PDE-LDDMM, def. st. eq.	RK	18079	2934.80 ± 121.20
J. EPDiff PDE-LDDMM	SL-RK	13801	337.88 ± 126.20
J. EPDiff PDE-LDDMM, st. eq.	SL-RK	14477	490.79 ± 90.80
J. EPDiff PDE-LDDMM, def. st. eq.	SL-RK	14659	540.99 ± 84.97
BL Zhang et al. IJCV 2018 32x	RK	1345	229.40 ± 0.25
BL St. PDE-LDDMM 40x	RK	5709	312.45 ± 5.22
BL St. PDE-LDDMM st. eq. 32x	RK	4743	315.00 ± 2.73
BL St. PDE-LDDMM def. st. eq. 32x	RK	1819	377.56 ± 4.26
BL St. PDE-LDDMM 40x	SL-RK	2685	68.66 ± 1.32
BL St. PDE-LDDMM st. eq. 32x	SL-RK	2877	80.76 ± 0.35
BL St. PDE-LDDMM def. st. eq. 32x	SL-RK	2365	116.99 ± 1.04
BL NSt. PDE-LDDMM 40x	RK	6657	825.15 ± 19.93
BL NSt. PDE-LDDMM, st. eq. 32x	RK	4789	535.52 ± 279.65
BL NSt. PDE-LDDMM, def. st. eq. 32x	RK	1863	905.48 ± 25.13
BL NSt. PDE-LDDMM 40x	SL-RK	6131	158.79 ± 15.29
BL NSt. PDE-LDDMM st. eq. 32x	SL-RK	6171	159.49 ± 20.59
BL NSt. PDE-LDDMM def. st. eq. 32x	SL-RK	5577	249.60 ± 10.85
BL J. EPDiff PDE-LDDMM 32x	RK	3241	540.83 ± 7.14
BL J. EPDiff PDE-LDDMM, st. eq. 32x	RK	1903	439.81 ± 5.11
BL J. EPDiff PDE-LDDMM, def. st. eq. 32x	RK	1879	488.74 ± 7.61
BL J. EPDiff PDE-LDDMM 32x	SL-RK	3219	172.04 ± 3.53
BL J. EPDiff PDE-LDDMM, st. eq. 32x	SL-RK	3027	197.15 ± 3.10
BL J. EPDiff PDE-LDDMM, def. st. eq. 32x	SL-RK	3001	199.72 ± 4.58

with initial condition $X(0) = x$. The band-limited transport equation is solved in the Eulerian grid

$$\tilde{D}_t \tilde{u}(\widetilde{X}(t), t) = \tilde{f}(\tilde{u}(\widetilde{X}(t), t), \tilde{v}(t, \widetilde{X}(t))). \tag{68}$$

The differential equations written in the shape of Eq. (68) and needed for the application of SL schemes can be obtained by projecting the equations obtained for the problem in the spatial domain to the band-limited domain. Table 2 gathers the expressions of these differential equations.

5. Implementation details

In this work, the methods are regularized with $L = (Id - \alpha\Delta)^s$ and the regularization parameters $\sigma = 1.0$, $\alpha = 0.0025$, and $s = 2$ in a unit-domain discretization of the image domain Ω [17]. These values were previously selected as optimal in [25]. Gauss–Newton–Krylov optimization is run a maximum of 10 iterations and a maximum of 5 CG iterations. These parameters were selected as optimal in our previous works [25,38,40]. Gradient-Descent optimization of the benchmark MCC methods is run a maximum of 50 iterations for a fair comparison. We use the stopping conditions proposed in [28].

The BL PDE-LDDMM experiments were performed with band sizes of $40 \times 40 \times 40$ for original BL PDE-LDDMM, and $32 \times 32 \times 32$ for BL PDE-LDDMM based on the state and on the deformation state equations. This selection was found as optimal for each method in our previous work [38,39]. The BL EPDiff PDE-LDDMM experiments were performed with band sizes ranging from $32 \times 32 \times 32$ to $64 \times 64 \times 64$.

For PDE integration, the computation of differentials is approached using Fourier spectral methods as an alternative to commonly used finite difference approximations [47]. Spectral differentiation was introduced in diffeomorphic registration literature in [28]. The RK method used in this work is Bogacki–Shampine Runge–Kutta of order 3. The solutions are computed at the Chebyshev–Gauss–Lobatto discretization of the temporal domain [0, 1]. For SL-RK integration, the size of the time sampling n_t was selected equal to 5 for all the methods. For RK integration, n_t was selected from 25 to 50, depending on stability issues. The Courant–Friedrichs–Lewy (CFL) condition was monitored to this end during the testing phase of our work. Table 4 in the Results section details the specific value of n_t used for each method. Since v_t is computed in the RK domain, a time sampling of v_t is needed for SL-RK integration. In this work, we use a piecewise time sampling. In addition, we use cubic interpolation for the estimation of the velocity field at points that do not belong to the Eulerian grid, as suggested in [35].

The experiments were run on a computer equipped with one NVidia Titan RTX with 24 GBS of video memory and an Intel Core i7 with 64 GBS of DDR3 RAM. The codes were developed in the GPU with Matlab 2017a and Cuda 8.0. Since Matlab lacks a 3D GPU cubic interpolator,

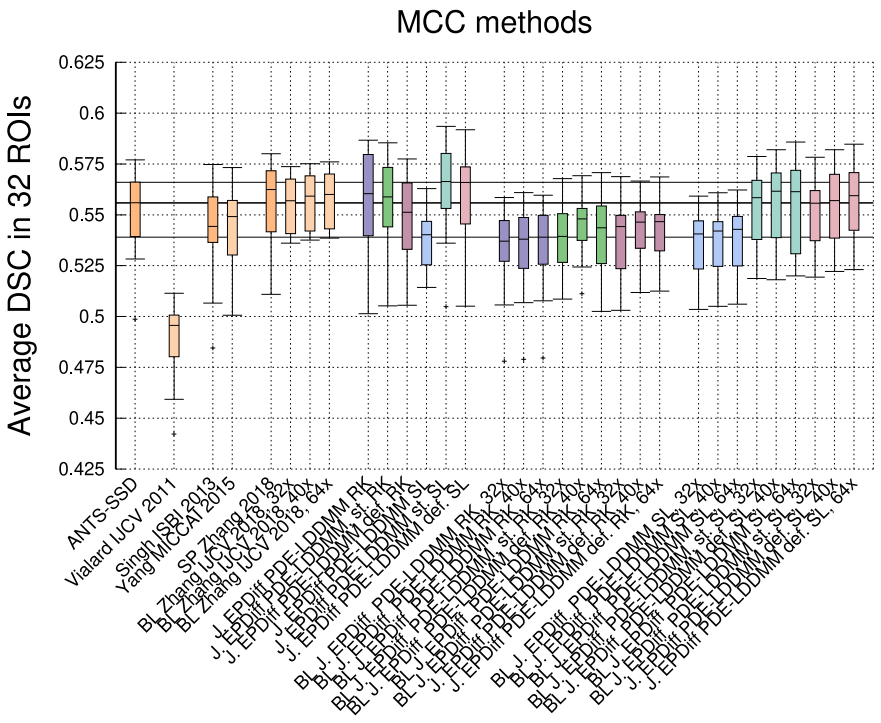

Fig. 1. Evaluation of MCC PDE-LDDMM methods. Volume overlap obtained by the registration methods measured in terms of the DSC. Box and whisker plots show the distribution of the DSC values averaged over the 32 NIREP manual segmentations. The whiskers indicate the minimum and maximum of the DSC values. The horizontal black lines indicate the first and third quartiles of ANTS-SSD method.

we implemented in a Cuda MEX file the GPU cubic interpolator with prefiltering proposed in [48].

6. Results

In this section, we evaluate the performance of our proposed variants of Jacobi EPDiff PDE-LDDMM formulated in the spatial and BL domains with SL-RK integration. In addition, we compare the computational efficiency achieved by SL-RK integration with respect to RK integration and by the BL parameterization with respect to the spatial parameterization.

As a benchmark for the evaluation, we include the results of:

- SyN diffeomorphic registration with L^2-based image similarity (ANTS-SSD) [49].
- PDE-LDDMM [29,35,38,39].
- Vialard et al. EPDiff PDE-LDDMM method (Vialard IJCV 2011) [19].
- The spatial and BL versions of Zhang and Fletcher method (Zhang IJCV 2018) [24,42].
- The EPDiff PDE-LDDMM methods in Singh et al. and Yang et al. [22,23] (Singh ISBI 2013 and Yang MICCAI 2015). Although the method in Yang et al. is for registration uncertainty estimation, the equations can be used for diffeomorphic registration. The adapted method was provided in [25] and it can be seen as a version of Singh et al. with Gauss–Newton–Krylov optimization.
- The Jacobi EPDiff PDE-LDDMM method with RK integration proposed in [25].

Table 3 details the PDE-LDDMM methods compared in this work.

The experiments have been conducted on the Non-Rigid Image Registration Evaluation Project database (NIREP) [50]. This database has been extensively used in the evaluation of registration methods [51]. Indeed, NIREP is the dataset of choice for the evaluation of the most recently proposed PDE-LDDMM methods [25,29,38]. Due to the large computational requirements of the benchmark methods, we have used a subsampled version of NIREP with volumes of size $180 \times 210 \times 180$. As a preprocessing step, the images were affinely registered to a common template before non-rigid registration using the algorithms available in ITK (www.itk.org). The first subject was registered to every other subject in the database, yielding 15 registrations for each method.

6.1. Quantitative results

Table 4 shows, averaged by the number of experiments, the relative image similarity error, the relative gradient magnitude, and the minimum and maximum of the Jacobian determinant obtained after registration for the benchmark and the proposed methods. The image similarity error is measured in terms of the L^2 Mean Squared Error relative to the first iteration $MSE_{rel} = \|m(1) - I_1\|_{L^2} / \|I_0 - I_1\|_{L^2}$. The relative gradient corresponds with $\|g\|_{\infty,rel} = \|\nabla_v E(v^n)\|_\infty / \|\nabla_v E(v^0)\|_\infty$ for the methods formulated in the space of time-varying or stationary velocity fields, $\|g\|_{\infty,rel} = \|\nabla_{v_0} E(v_0^n)\|_\infty / \|\nabla_{v_0} E(v_0^0)\|_\infty$ for the methods formulated in the space of initial velocity fields, and $\|g\|_{\infty,rel} = \|\nabla_{\tilde{v}} E(\tilde{v}^n)\|_\infty / \|\nabla_{\tilde{v}} E(\tilde{v}^0)\|_\infty$ or $\|g\|_{\infty,rel} = \|\nabla_{\tilde{v}_0} E(\tilde{v}_0^n)\|_\infty / \|\nabla_{\tilde{v}_0} E(\tilde{v}_0^0)\|_\infty$ for the BL parameterization.

6.1.1. Results of the spatial methods

Our proposed variants II and III of Jacobi EPDiff PDE-LDDMM overpassed all the benchmark MCC methods in terms of the obtained MSE_{rel}. From the benchmark PDE-LDDMM methods, the best performing variant in terms of MSE_{rel} was Variant III. In contrast, from the proposed Jacobi EPDiff PDE-LDDMM methods, the best performing variant turned out to be Variant II. The mean MSE_{rel} value of the best performing Jacobi EPDiff PDE-LDDMM method was 16.52%. This quantity is close to the 16.10% obtained by the best benchmark PDE-LDDMM method. For variants II and III Jacobi EPDiff PDE-LDDMM SL-RK improved the performance of RK integration. The $\|g\|_{\infty,rel}$ values showed an acceptable convergence behavior, except in three cases. All the methods provided diffeomorphic solutions for the selected parameters ($\min(J(\phi(1)) > 0$).

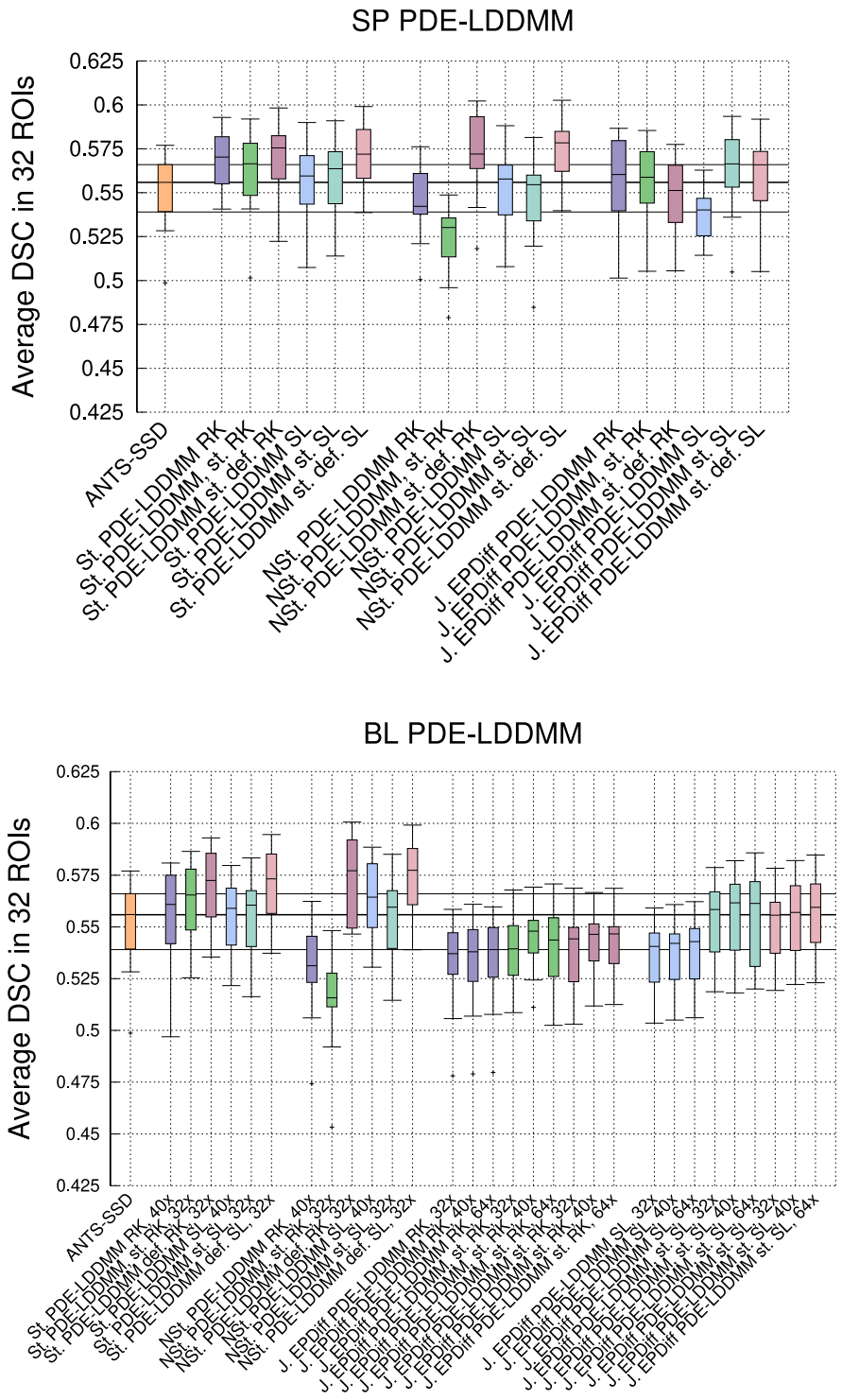

Fig. 2. Comparison of spatial and band-limited PDE-LDDMM methods with Jacobi EPDiff PDE-LDDMM.

6.1.2. Results of the BL methods

The MSE_{rel} values obtained by the BL methods were close to the values obtained by the corresponding spatial methods. The selection of the dimension of the BL domain did not impact much the achieved MSE_{rel} value. As happened with the methods in the spatial domain, our proposed variants II and III of BL Jacobi EPDiff PDE-LDDMM also overpassed all the benchmark MCC methods. The best performing variants were Variant III for the BL PDE-LDDMM benchmark methods, and Variant II for BL Jacobi EPDiff PDE-LDDMM. The mean MSE_{rel} value of the best performing BL Jacobi EPDiff PDE-LDDMM method was 16.65%. This quantity is in the same order as the best performing PDE-LDDMM benchmark method in both the spatial and BL domains. The improvement of SL-RK integration with respect to RK shown for the spatial methods was also consistent with the BL methods. The $\|g\|_{\infty,rel}$ values also showed an acceptable convergence behavior in all cases and all the BL methods provided diffeomorphic solutions.

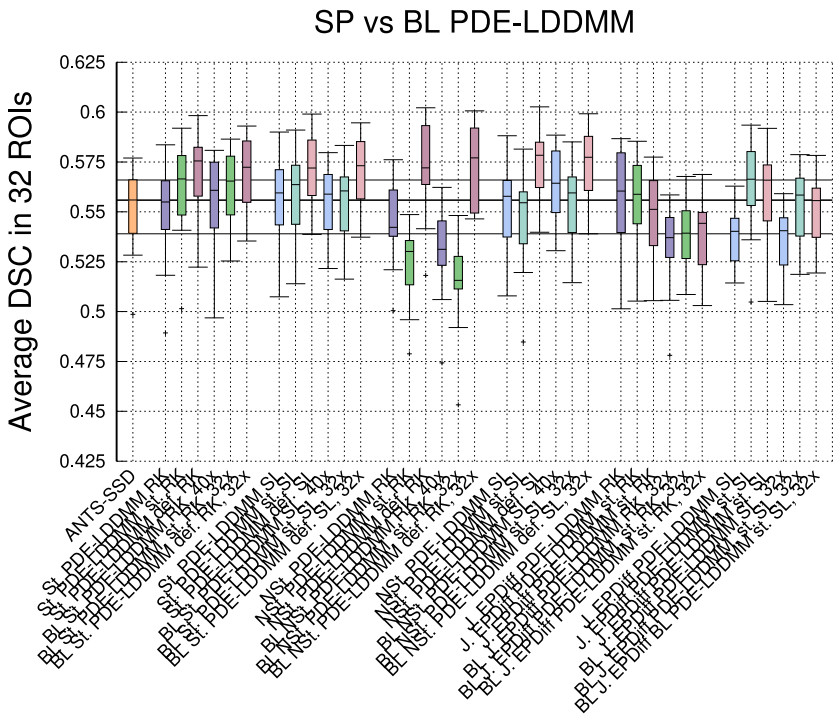

Fig. 3. Comparison of spatial vs band-limited PDE-LDDMM methods and Jacobi EPDiff PDE-LDDMM.

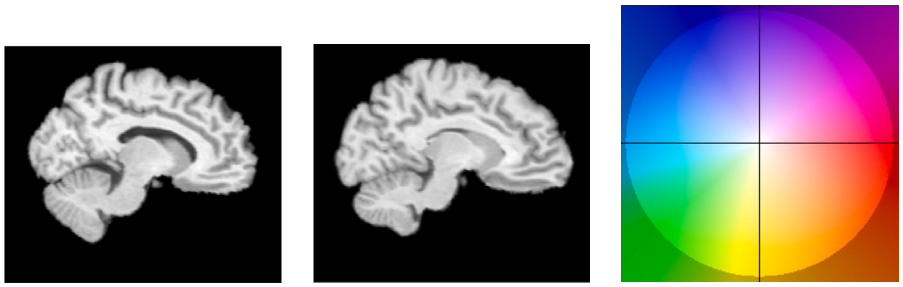

Fig. 4. Sagittal view of the source and target images of the results shown in Section 6.3, and color wheel used for the vector fields representation.

6.2. Evaluation

The evaluation of the proposed methods and the comparison with the benchmarks have been performed similarly to [25,39]. The evaluation is based on the accuracy of the registration results for template-based segmentation of sufficiently small and localized labeled regions, a criterion extensively used in the evaluation of registration methods [51–53]. We use the manual segmentations provided with the NIREP database as a gold standard. Dice Similarity Coefficient (DSC) is selected as the performance metric. Given S and T two segmented structures, DSC is defined as

$$DSC(S,T) = 2Vol(S \cap T)/(Vol(S) + Vol(T)). \tag{69}$$

This metric provides the value of 1 if S and T exactly overlap and gradually decreases towards 0 depending on the overlap of the two volumes. In this work, the DSC is computed between the warped and the corresponding manual target segmentations. As a lower bound baseline, the average DSC value before deformable registration is equal to 43.75%.

It should be noticed that some works have reported DSC values ranging from 75% to 80% in this dataset [36]. However, the computation of the DSC values has been performed in the total brain volume without having into account the registration accuracy obtained in each particular subregion. Our approach for computing the DSC values follows the recommendations used in the state of the art of non-rigid registration evaluation [51–53]. Our results should be not compared with a benchmark of 75% or 80% but with the results obtained by a well-established diffeomorphic registration method. For example, the average DSC value achieved by SyN diffeomorphic registration with L^2-based image similarity (ANTS-SSD) equals to 55.59% in this dataset [25,49]. We have selected this value as a benchmark of good registration accuracy for methods with L^2-based image similarity.

Figs. 1 and 2 show the statistical distribution of the $DSCs$ obtained after the registration across the 32 segmented structures. The results have been grouped into three different categories of the LDDMM-Verse: MCC methods, PDE-LDDMM methods, and BL PDE-LDDMM methods. In addition, Fig. 3 compares the performance of the spatial vs the BL methods for the family of PDE-LDDMM methods.

6.2.1. Evaluation of the MCC methods

From the results of the benchmark MCC methods in Fig. 1, it is remarkable the poor performance of Vialard et al. method. Singh ISBI 2013 and Yang MICCAI 2015 methods performed similarly. The first method is nearly a gradient-descent version of the second method. Zhang et al. performed similarly to BL Zhang et al. for the selected BL sizes.

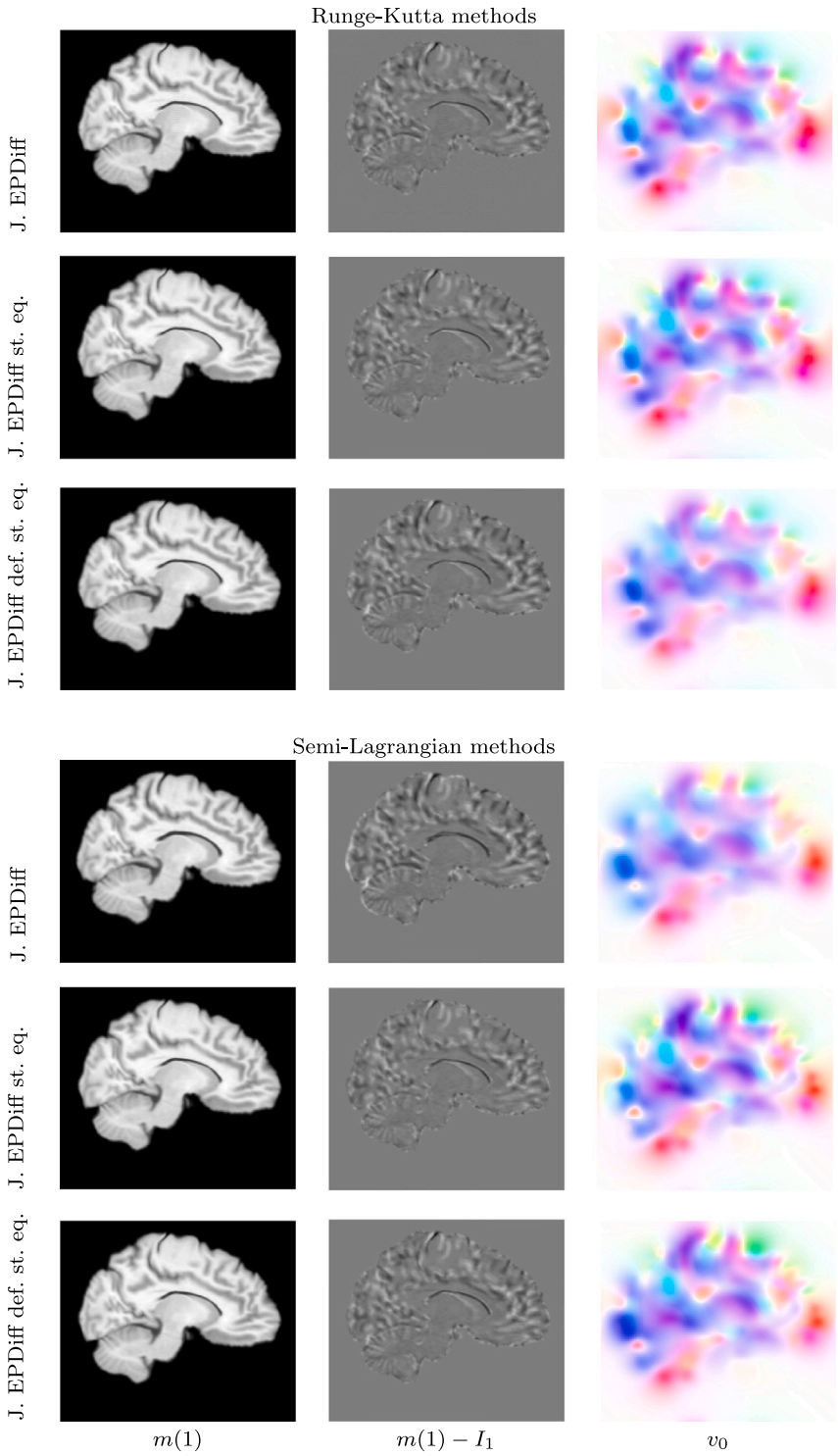

Fig. 5. Jacobi EPDiff PDE-LDDMM methods. Sagittal view of the warped sources, the intensity differences, and the initial velocity fields after registration.

The best performing MCC method was our proposed Jacobi EPDiff PDE-LDDMM st. (Variant II) with SL-RK integration. In fact, Variant II and Variant III in the spatial domain with SL-RK integration outperformed the benchmark MCC methods. Variant I and Variant II of Jacobi EPDiff PDE-LDDMM with RK integration stayed in a competitive position.

Regarding the BL versions of Jacobi EPDiff PDE-LDDMM, the use of the BL parameterization degraded the performance of RK integration under ANTS-SSD baseline. However, the performance of BL Jacobi EPDiff PDE-LDDMM st. and st. def. (variants II and III) with SL-RK integration was similar to the best benchmark MCC methods.

6.2.2. *Evaluation of the PDE-LDDMM methods*

Among the PDE-LDDMM methods in Fig. 2, only NSt. PDE-LDDMM st. (Variant II) with RK integration and Jacobi EPDiff PDE-LDDMM (Variant I) with SL integration underperformed ANTS-SSD. The DSC results corroborated that PDE-LDDMM st. def. (Variant III) was the best performing method among the benchmark PDE-LDDMM methods and that PDE-LDDMM st. (Variant II) was the best performing method

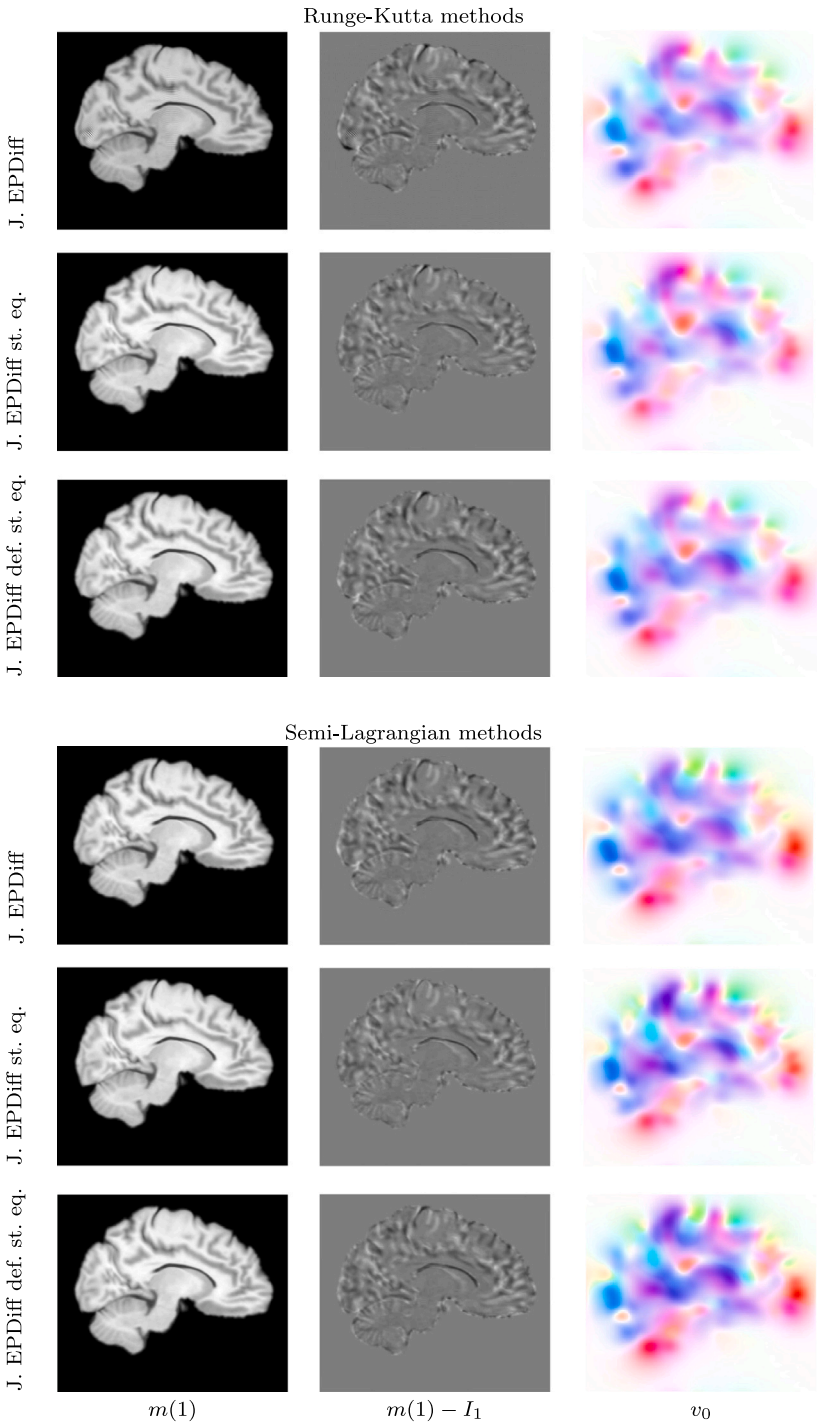

Fig. 6. BL Jacobi EPDiff PDE-LDDMM methods. Sagittal view of the warped sources, the intensity differences, and the initial velocity fields after registration.

among the proposed Jacobi EPDiff PDE-LDDMM methods, as happened with the MSE_{rel} results.

Jacobi EPDiff PDE-LDDMM (Variant I) with SL-RK integration performed slightly under the corresponding method with RK integration. A similar observation can be drawn from St. PDE-LDDMM (Variant I) with SL-RK and RK integration. Therefore, it seems that for the original PDE-LDDMM formulation [29,35], the accuracy provided by SL-RK integration is lower than with explicit schemes. On the contrary, Jacobi EPDiff PDE-LDDMM st. and st. def. (variants II and III) with SL-RK integration slightly outperformed their corresponding variant with RK integration.

The stationary methods and NSt. PDE-LDDMM st. def. (Variant III) outperformed Jacobi EPDiff PDE-LDDMM. This may be due to the EPDiff-constraint imposes a more restrictive physical model in the space of solutions and, in consequence, the performance obtained within this evaluation framework is slightly degraded compared with under-constrained LDDMM methods. However, EPDiff constrained methods are preferable in Computational Anatomy applications since they provide true geodesic solutions while NSt. PDE-LDDMM provides approximated geodesic solutions and St. PDE-LDDMM provides solutions belonging to one-parameter subgroups, not geodesics.

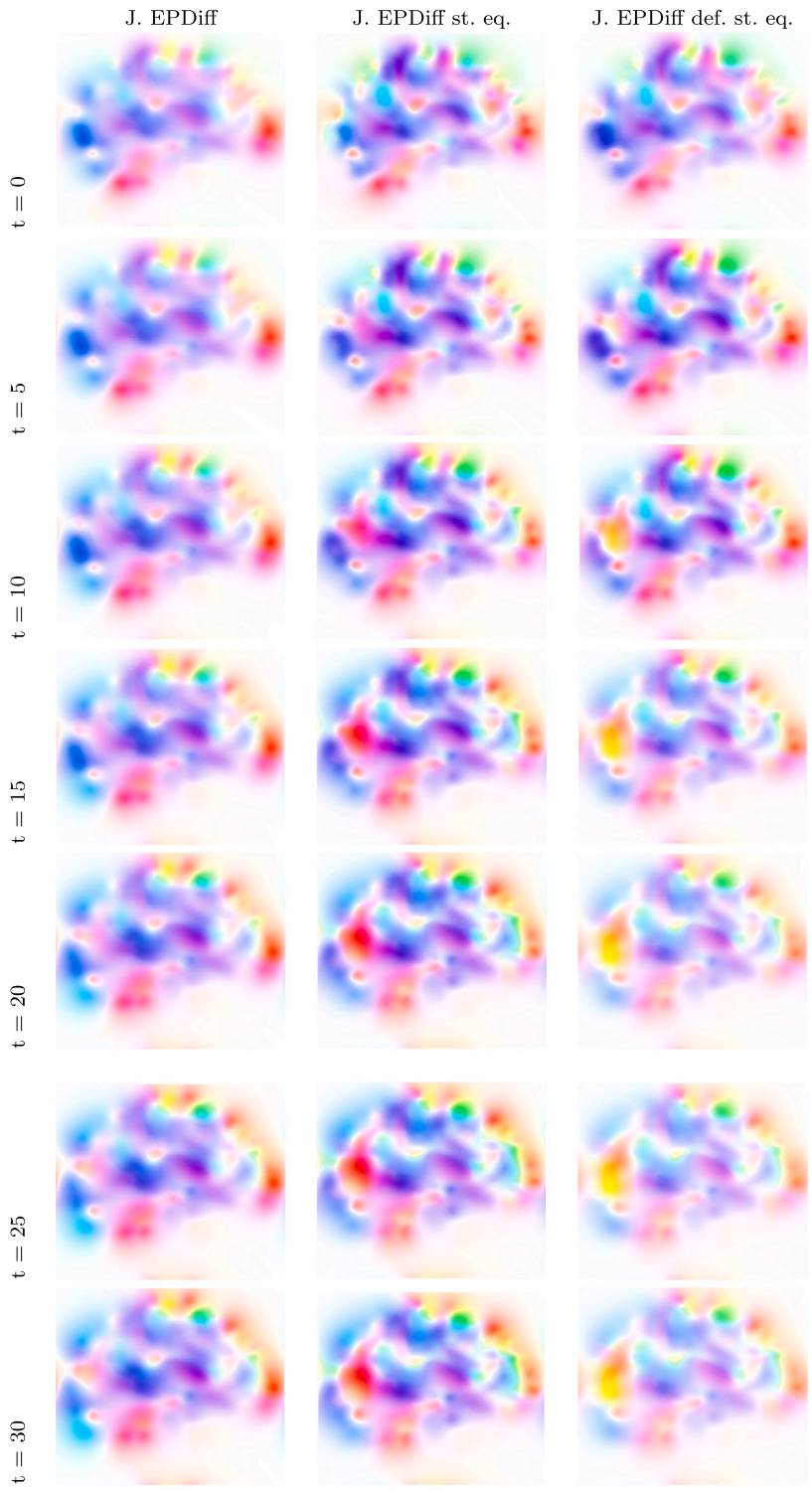

Fig. 7. Proposed Jacobi EPDiff PDE-LDDMM methods. Sagittal view of the velocity field flow v_t computed from v_0 after registration.

6.2.3. Evaluation of the BL PDE-LDDMM methods

It can be appreciated in Fig. 3 that the performance of the best performing benchmark PDE-LDDMM methods (variants II and III) was slightly degraded with the use of the BL parameterization, while the use of the BL parameterization in Jacobi PDE-LDDMM with RK integration degraded their performance under ANTS-SSD. For variants II and III of BL Jacobi PDE-LDDMM with SL-RK integration, the degradation due to the BL parameterization was admissible, yielding an acceptable performance comparable to ANTS-SSD, competitive with the best benchmark MCC methods, and slightly under the best performing spatial Jacobi EPDiff PDE-LDDMM methods.

6.3. Qualitative results

For a qualitative assessment of the proposed registration methods, we show the registration results obtained by our proposed methods in a selected experiment representative of a difficult deformable registration problem. Fig. 4 shows the source and target images. Figs. 5

and 6 show the warped images, the difference between the warped and the target images after registration and the initial velocity field. There is no appreciable difference between the warped images and the differences of RK and SL-RK integration for the alternative Jacobi EPDiff PDE-LDDMM methods based on the state and the deformation state equations (variants II and III). However, these variants outperform original Jacobi EPDiff PDE-LDDMM (Variant I) in the case of SL-RK integration. This result is in agreement with the MSE_{rel} results shown in the quantitative experiments and the DSC values in the evaluation results. A similar visual assessment can be performed for the BL Jacobi EPDiff PDE-LDDMM methods. Fig. 7 shows the velocity field flow v_t computed from v_0 using the EPDiff-equation for Jacobi EPDiff PDE-LDDMM methods with SL-RK integration. It can be appreciated that original Jacobi EPDiff PDE-LDDMM is not able to capture as low-level details as the two alternative variants. This is the reason for their improved performance.

6.4. Computational complexity

Table 5 shows the computational complexity of the methods at the resolution level of $180 \times 210 \times 180$. From the spatial methods, only Zhang IJCV 2018 and St. PDE-LDDMM with SL-RK integration would fit in a GPU with less than 10 GBS. The BL parameterization achieved a considerable memory reduction over spatial-based methods. For the spatial methods, SL-RK integration achieved a substantial memory reduction over RK integration. In contrast, the BL methods with SL-RK integration did not show an effective memory reduction over RK integration in some cases. This is because of the need for storing the departure points $X(t)$ needed for SL integration. Regarding the computational time, our proposed BL J. EPDiff PDE-LDDMM methods significantly outperformed all the MCC benchmark methods, even BL Zhang IJCV 2018, which uses gradient-descent optimization.

7. Conclusions

In this work, we have proposed three efficient variants of PDE-constrained LDDMM formulated in the space of initial velocity fields under the EPDiff momentum conservation constraint. The proposed methods start from previously proposed Jacobi EPDiff PDE-LDDMM method [25] and are formulated with the best variational formulations in [34,39,43]. In our methods, the gradient and the Hessian-vector products are computed in the space of final velocity fields and transported to the space of initial velocity fields using the adjoint Jacobi equations and their incremental counterparts. Efficiency is achieved through Semi-Lagrangian Runge–Kutta PDE integration and the band-limited parameterization. We have derived the equations for Semi-Lagrangian Runge–Kutta integration using the terms of the expansion of the EPDiff equation and the adjoint action to write the left-hand side of the equations in Semi-Lagrangian form both in the spatial and the BL domains.

The proposed methods have been compared with the most relevant MCC methods in the state of the art and the previously proposed PDE-LDDMM methods most related to our work. The evaluation has shown that the variants of Jacobi EPDiff PDE-LDDMM based on the state and the deformation state equations with SL-RK integration significantly outperform the benchmark MCC methods. It is remarkable that, for the parameterization in the spatial domain, the performance of our best performing proposed methods is similar to PDE-LDDMM [28] despite the restriction in the degrees of freedom imposed by the momentum conservation constraint. For the BL parameterization, our best-proposed methods have performed slightly under the best-performing BL PDE-LDDMM methods, with an acceptable performance comparable to ANTS-SSD and competitive with the best benchmark MCC methods.

Thanks to the proposed SL-RK integration and BL parameterization, the memory of the proposed methods has been considerably reduced to a memory usage that allows running our methods completely in the VRAM of commodity GPUs (< 4GBS). Also, the computation time requirements are significantly lower than the time required by Runge–Kutta integration methods. Overall, memory requirements were much lower than spatial MCC benchmark methods and time requirements were even smaller than Zhang et al. BL MCC benchmark, an MCC method outstanding by its efficiency [24].

From these results, Jacobi EPDiff PDE-LDDMM based on the state equation (the second variant) would be our recommendation for Computational Anatomy applications requiring geodesics. This selection is in contrast to the one driven for PDE-LDDMM in [39,40], where the method based on the deformation state equation (the third variant) was selected due to its best performance.

In future work, we will study the performance of our most accurate variants of Jacobi EPDiff PDE-LDDMM in the efficient construction of physically meaningful transversal and longitudinal models of shape variability for Computational Anatomy applications. An interesting application to start from could be cardiac motion analysis with nearly incompressible geodesics. In addition, we will investigate whether our proposed Jacobi EPDiff PDE-LDDMM yields any advantage in the diagnosis and prognosis of Alzheimer's disease with the deep network architecture of Spasov et al. [54] as obtained with the third variant of stationary PDE-LDDMM in [55].

Declaration of competing interest

The authors declare that they have no known competing financial interests or personal relationships that could have appeared to influence the work reported in this paper.

Acknowledgments

The author would like to acknowledge the anonymous reviewers for their revision of the manuscript. This work was partially supported by the national research grants TIN2016-80347-R (DIAMOND project) and PID2019-104358RB-I00 (DL-Aging project), Government of Aragon Group Reference $T64\_20R$ (COS2MOS research group), and NVIDIA through the Barcelona Supercomputing Center (BSC) GPU Center of Excellence.

Appendix

To apply SL-RK integration, the differential equations involved in the different variants of Jacobi EPDiff PDE-LDDMM need to be written in the shape of Eq. (64). This appendix gathers the derivation of the PDEs for the methods formulated in the spatial domain. The derivation of the PDEs in the band-limited domain can be obtained straightforwardly. The resulting equations are gathered in Tables 1 and 2.

EPDiff equation and incremental counterpart

The EPDiff equation computes the velocity field v, needed to solve the characteristic equation. Therefore, it cannot be solved using SL-RK schemes. The incremental EPDiff equation can be written in the form

$$\partial_t L\delta v_t + ad^*_{\delta v_t} L v_t + (Dv_t)^T L\delta v_t + D(L\delta v_t)v_t + L\delta v_t \nabla \cdot v_t = 0 \tag{70}$$

using the expansion of the EPDiff equation (Eq. (6)). Grouping the first and fourth terms into $D_t L\delta v_t$, moving the remaining terms to the right hand side, and applying K yield

$$D_t\delta v_t = -ad^{\dagger}_{\delta v_t} v_t - K((Dv_t)^T L\delta v_t + L\delta v_t \nabla \cdot v_t). \tag{71}$$

State and deformation state equations and incremental counterparts

The state and the deformation state equations are already written in the form of Eq. (64). For the incremental counterparts, it is enough to group the first and second terms into $D_t\delta m(t)$ and $D_t\delta\phi(t)$, respectively, and move the remaining term to the right-hand side, yielding

$$D_t\delta m(t) = -\nabla m(t) \cdot \delta v_t \, D_t\delta\phi(t) = -D\phi(t) \cdot \delta v_t. \tag{72}$$

Adjoint Jacobi equations

The U-Adjoint Jacobi equation can be written in the form

$$\partial_t LU_t + (Dv_t)^T LU_t + D(LU_t)v_t + LU_t \nabla \cdot v_t = 0 \tag{73}$$

using the expansion of the EPDiff equation (Eq. (6)). Grouping the first and third terms into $D_t LU_t$, moving the remaining terms to the right hand side, and applying K we get

$$D_t U_t = -K((Dv_t)^T LU_t + LU_t \nabla \cdot v_t). \tag{74}$$

The w-Adjoint Jacobi equation can be written in the form

$$\partial_t w_t - Dv_t w_t + Dw_t v_t + ad^{\dagger}_{w_t} v_t + U_t = 0 \tag{75}$$

using the expression of the adjoint action. Grouping the first and third terms into $D_t w_t$ and moving the remaining terms to the right hand side, we get

$$D_t w_t = Dv_t w_t - ad^{\dagger}_{w_t} v_t - U_t. \tag{76}$$

Incremental adjoint Jacobi equations

The δU-Adjoint Jacobi equation can be derived similarly to the U-Adjoint Jacobi equation since both equations differ in the term $ad^{\dagger}_{\delta v_t} U_t$. Thus,

$$D_t \delta U_t = -K((Dv_t)^T L\delta U_t + L\delta U_t \nabla \cdot v_t) - ad^{\dagger}_{\delta v_t} U_t. \tag{77}$$

Likewise, the δw-Adjoint Jacobi equation can be driven similarly to the w-Adjoint Jacobi equation, yielding

$$D_t \delta w_t = Dv_t \delta w_t - ad^{\dagger}_{\delta w_t} v_t - \delta U_t = 0. \tag{78}$$

References

[1] M.I. Miller, Computational anatomy: shape, growth, and atrophy comparison via diffeomorphisms, Neuroimage 23 (2004) 19–33.

[2] M.I. Miller, A. Qiu, The emerging discipline of Computational Functional Anatomy, Neuroimage 45 (1) (2009) 16–39.

[3] D.W. Thompson, On Growth and Form, Cambridge University Press, 1917.

[4] M. Zhang, P.T. Fletcher, Bayeslan principal geodesic analysis for estimating intrinsic diffeomorphic image variability, Med. Image Anal. 25 (1) (2015) 37–44.

[5] N. Singh, J. Hinkle, S. Joshi, P.T. Fletcher, Hierarchical geodesic models in diffeomorphisms, Int. J. Comput. Vis. 117 (1) (2016) 70–92.

[6] M.I. Miller, S. Arguillere, D. Tward, L. Younes, Computational anatomy and diffeomorphometry: A dynamical systems model of neuroanatomy in the soft condensed matter continuum, Technology 2 (1) (2014) 36.

[7] A. Sotiras, C. Davatzikos, N. Paragios, Deformable medical image registration: A survey, IEEE Trans. Med. Imaging 32 (7) (2013) 1153–1190.

[8] L. Younes, Shapes and Diffeomorphisms, Springer-Verlag, Berlin, Germany, 2010.

[9] M.M. Rohe, M. Datar, T. Heimann, M. Sermesant, X. Pennec, SVF-Net: Learning deformable image registration using shape matching, in: Proc. of the 20th International Conference on Medical Image Computing and Computer Assisted Intervention, MICCAI'17, Lecture Notes in Computer Science, vol 10433, 2017, pp. 266–274.

[10] X. Yang, R. Kwitt, M. Styner, M. Niethammer, Quicksilver: Fast predictive image registration - a deep learning approach, Neuroimage 158 (2017) 378–396.

[11] A.V. Dalca, G. Blakrishnan, J. Guttag, M. Sabuncu, Unsupervised learning for fast probabilistic diffeomorphic registration, in: Proc. of the 21th International Conference on Medical Image Computing and Computer Assisted Intervention MICCAI'18, Lecture Notes in Computer Science, vol. 11070, 2018, pp. 729–738.

[12] G. Balakrishnan, A. Zhao, M.R. Sabuncu, J. Guttag, A.V. Dalca, VoxelMorph: A learning framework for deformable medical image registration, IEEE Trans. Med. Imaging 38 (8) (2019) 1788–1800.

[13] J. Krebs, H. Delingetter, B. Mailhe, N. Ayache, T. Mansi, Learning a probabilistic model for diffeomorphic registration, IEEE Trans. Med. Imaging (2019).

[14] J. Fan, X. Cao, P.T. Yap, D. Shen, BIRNet: brain image registration using dual-supervised fully convolutional networks, Med. Image Anal. 54 (2019) 193–206.

[15] J. Wang, M. Zhang, DeepFLASH: an efficient network for learning-based medical52image registration, in: Proc. of the IEEE Conference on Computer Vision and Pattern Recognition CVPR'20, 2020.

[16] M. Vaillant, M.I. Miller, L. Younes, A. Trouve, Statistics on diffeomorphisms via tangent space representations, IEEE Trans. Med. Imaging 23 (2004) 161–169.

[17] M.F. Beg, M.I. Miller, A. Trouve, L. Younes, Computing large deformation metric mappings via geodesic flows of diffeomorphisms, Int. J. Comput. Vis. 61 (2) (2005) 139–157.

[18] M.P. doCarmo, Differential Geometry of Curves and Surfaces, Prentice Hall, New Jersey, 1976.

[19] F.X. Vialard, L. Risser, D. Rueckert, C.J. Cotter, Diffeomorphic 3D image registration via geodesic shooting using an efficient adjoint calculation, Int. J. Comput. Vis. 97 (2) (2011) 229–241.

[20] M.I. Miller, A. Trouve, L. Younes, Geodesic shooting for computational anatomy, J. Math. Imaging Vision 24 (2006) 209–228.

[21] L. Younes, Jacobi fields in groups of diffeomorphisms and applications, Q. Appl. Math. 65 (2007) 113–134.

[22] N. Singh, J. Hinkle, S.C. Joshi, P.T. Fletcher, A vector momenta formulation of diffeomorphisms for improved geodesic regression and atlas construction, in: Proc. of the 10th IEEE International Symposium on Biomedical Imaging: from Nano To Macro, ISBI'12, 2013.

[23] X. Yang, M. Niethammer, Uncertainty quantification for LDDMM using a low-rank Hessian approximation, in: Proc. of the 18th International Conference on Medical Image Computing and Computer Assisted Intervention, MICCAI'16, Lecture Notes in Computer Science, vol. 9350, 2015, pp. 289–296.

[24] M. Zhang, T. Fletcher, Fast diffeomorphic image registration via Fourier-Approximated Lie algebras, Int. J. Comput. Vis. (2018).

[25] M. Hernandez, PDE-constrained LDDMM via geodesic shooting and inexact Gauss-Newton-Krylov optimization using the incremental adjoint Jacobi equations, Phys. Med. Biol. 64 (2) (2019).

[26] T. Mansi, X. Pennec, M. Sermesant, H. Delingette, N. Ayache, iLogDemons: A demons-based registration algorithm for tracking incompressible elastic biological tissues, Int. J. Comput. Vis. 92 (1) (2011) 92–111.

[27] L. Risser, F.X. Vialard, H.Y. Baluwala, J.A. Schnabel, Piecewise-diffeomorphic image registration: Application to the motion correction of 3D CT lung images using sliding conditions, Med. Image Anal. 17 (2) (2012) 182–193.

[28] A. Mang, G. Biros, An inexact Newton-Krylov algorithm for constrained diffeomorphic image registration, SIAM J. Imaging Sci. 8 (2) (2015) 1030–1069.

[29] A. Mang, G. Biros, Constrained H1 regularization schemes for diffeomorphic image registration, SIAM J. Imaging Sci. 9 (3) (2016) 1154–1194.

[30] A. Mang, L. Ruthotto, A Lagrangian Gauss Newton Krylov solver for mass- and intensity-preserving diffeomorphic image registration, SIAM J. Sci. Comput. 39 (5) (2017) B860–B885.

[31] C. Hogea, C. Davatzikos, G. Biros, Brain-tumor interaction biophysical models for medical image registration, SIAM J. Imaging Sci. 30 (2008) 3050–3072.

[32] A. Mang, A. Toma, T.A. Schuetz, S. Becker, T. Eckey, C. Mohr, D. Petersen, T.M. Buzug, Biophysical modeling of brain tumor progression: From unconditionally stable explicit time integration to an inverse problem with parabolic PDE constraints for model calibration, Med. Phys. 39 (7) (2012) 4444–4460.

[33] A. Gholami, A. Mang, G. Biros, An inverse problem formulation for parameter estimation of a reaction-diffusion model for low grade gliomas, J. Math. Biol. 72 (1) (2016) 409–433.

[34] G.L. Hart, C. Zach, M. Niethammer, An optimal control approach for deformable registration, in: Proc. of the IEEE Conference on Computer Vision and Pattern Recognition, CVPR'09, 2009.

[35] A. Mang, G. Biros, A semi-Lagrangian two-level preconditioned Newton-Krylov solver for constrained diffeomorphic image registration, SIAM J. Sci. Comput. 39 (6) (2017) B1064–B1101.

[36] A. Mang, K. Scheufele, A. Gholami, C. Davatzikos, G. Biros, M. Mehl, Coupling brain-tumor biophysical models and diffeomorphic image registration, Comput. Methods Appl. Mech. Engrg. 347 (2019) 533–567.

[37] M. Brunn, N. Himthani, G. Biros, M. Mehl, Multi-node multi-GPU diffeomorphic image registration for large-scale imaging problems, in: International Conference on Supercomputing, 2020.

[38] M. Hernandez, Band-limited stokes large deformation diffeomorphic metric mapping, IEEE J. Biom. Health Inf. 23 (1) (2019).

[39] M. Hernandez, A comparative study of different variants of Newton-Krylov PDE-constrained Stokes-LDDMM parameterized in the space of band-limited vector fields, SIAM J. Imaging Sci. 12 (2) (2019).

[40] M. Hernandez, Combining the band-limited parameterization and Semi-Lagrangian Runge–Kutta integration for efficient PDE-constrained LDDMM, J. Math. Imaging Vision 63 (2021) 555–579.

[41] D.D. Holm, J.E. Marsden, T.S. Ratiu, The Euler-Poincare equations and semidirect products with applications to continuum theories, Adv. Math. 137 (1998) 1–81.

[42] M. Zhang, P.T. Fletcher, Finite-Dimensional Lie algebras for fast diffeomorphic image registration, in: Proc. of International Conference on Information Processing and Medical Imaging, IPMI'15, Lecture Notes in Computer Science, 2015.

[43] T. Polzin, M. Niethammer, M.P. Heinrich, H. Handels, J. Modersitzki, Memory efficient LDDMM for lung CT, in: Proc. of the 19th International Conference on Medical Image Computing and Computer Assisted Intervention, MICCAI'16, in: Lecture Notes in Computer Science, 2014, pp. 28–36.

[44] M. Niethammer, Y. Huang, F.X. Vialard, Geodesic regression for image time series, in: Proc. of the 14th International Conference on Medical Image Computing and Computer Assisted Intervention, MICCAI'11, in: Lecture Notes in Computer Science, 2011.

[45] M. Hernandez, M.N. Bossa, S. Olmos, Registration of anatomical images using paths of diffeomorphisms parameterized with stationary vector field flows, Int. J. Comput. Vis. 85 (3) (2009) 291–306.

[46] D.X. Guo, A Semi-Lagrangian Runge-Kutta method for time-dependent partial differential equations, J. Appl. Anal. Comput. 3 (3) (2013) 251–263.
[47] L.N. Trefethen, Spectral Methods in Matlab, SIAM, Philadelphia, 2000.
[48] D. Ruijters, P. Thevenaz, GPU prefilter for accurate cubic B-spline interpolation, Comput. J. 55 (1) (2012) 15–20.
[49] B.B. Avants, C.L. Epstein, M. Grossman, J.C. Gee, Symmetric diffeomorphic image registration with cross-correlation: Evaluating automated labeling of elderly and neurodegenerative brain, Med. Image Anal. 12 (2008) 26–41.
[50] H. Song, G.E. Christensen, J.A. Hawley, Y. Wei, J.G. Kuhl, Evaluating image registration using NIREP, in: Proc. of 4th International Workshop on Biomedical Image Registration (WBIR'10), Lecture Notes in Computer Science, vol. 6204, 2010, pp. 140–150.
[51] Y. Ou, H. Akbari, M. Bilello, X. Da, C. Davatzikos, Comparative evaluation of registration algorithms in different brain databases with varying difficulty: results and insights, IEEE Trans. Med. Imaging 33 (10) (2014) 2039–2065.
[52] A. Klein, J. Andersson, B.A. Ardekani, J. Ashburner, B. Avants, M.C. Chiang, G.E. Christensen, D.L. Collins, J. Gee, P. Hellier, J.H. Song, M. Jenkinson, C. Lepage, D. Rueckert, P. Thompson, T. Vercauteren, R.P. Woods, J.J. Mann, R.V. Parsey, Evaluation of 14 nonlinear deformation algorithms applied to human brain MRI registration, Neuroimage 46 (3) (2009) 786–802.
[53] T. Rohlfing, Image similarity and tissue overlaps as surrogates for image registration accuracy: widely used but unreliable, IEEE Trans. Med. Imaging 31 (2) (2012) 153–163.
[54] S.E. Spasov, L. Passamonti, A. Duggento, P. Lio, N. Toschi, ADNI, A parameter-efficient deep learning approach to predict conversion from mild cognitive impairment to Alzheimer's disease, Neuroimage 189 (2019) 276–287.
[55] U. Ramon-Julvez, M. Hernandez, E. Mayordomo, ADNI, Analysis of the influence of diffeomorphic normalization in the prediction of stable vs progressive MCI conversion with convolutional neural networks, in: Proc. of the 17th IEEE International Symposium on Biomedical Imaging: from Nano to Macro, ISBI'20, 2020.

Monica Hernandez received the B.Sc. and M.Sc. degree in Mathematics from the University of Zaragoza in 2000. In 2008, she received the Ph.D. degree in Computer Science in the University of Zaragoza. Since 2011 she is associate professor in the Department of Informatics and Systems Engineering. Her current research interests include diffeomorphic registration, Computational Anatomy applications, and deep and interpretable machine learning towards the early diagnosis of neurodegenerative diseases.